
**AFRL-AFOSR-JP-TR-2023-0055**

# Vectoring of Plasma Thrusters for CubeSats

**Cater, John**
**THE UNIVERSITY OF AUCKLAND**
**24 PRINCES STREET**
**AUCKLAND, ,**
**NZL**

**01/12/2023**
**Final Technical Report**



Air Force Research Laboratory
Air Force Office of Scientific Research
Asian Office of Aerospace Research and Development
Unit 45002, APO AP 96338-5002

# REPORT DOCUMENTATION PAGE

**PLEASE DO NOT RETURN YOUR FORM TO THE ABOVE ORGANIZATION.**

| 1. REPORT DATE | 2. REPORT TYPE | 3. DATES COVERED | |
|---|---|---|---|
| 20230112 | Final | START DATE<br>20210501 | END DATE<br>20220430 |

**4. TITLE AND SUBTITLE**
Vectoring of Plasma Thrusters for CubeSats

| 5a. CONTRACT NUMBER | 5b. GRANT NUMBER | 5c. PROGRAM ELEMENT NUMBER |
|---|---|---|
| | FA2386-19-1-4012 | |
| **5d. PROJECT NUMBER** | **5e. TASK NUMBER** | **5f. WORK UNIT NUMBER** |
| | | |

**6. AUTHOR(S)**
John Cater

**7. PERFORMING ORGANIZATION NAME(S) AND ADDRESS(ES)**
THE UNIVERSITY OF AUCKLAND
24 PRINCES STREET
AUCKLAND
NZL

**8. PERFORMING ORGANIZATION REPORT NUMBER**

| 9. SPONSORING/MONITORING AGENCY NAME(S) AND ADDRESS(ES) | 10. SPONSOR/MONITOR'S ACRONYM(S) | 11. SPONSOR/MONITOR'S REPORT NUMBER(S) |
|---|---|---|
| AOARD<br>UNIT 45002<br>APO AP 96338-5002 | AFRL/AFOSR IOA | AFRL-AFOSR-JP-TR-2023-0055 |

**12. DISTRIBUTION/AVAILABILITY STATEMENT**
A Distribution Unlimited: PB Public Release

**13. SUPPLEMENTARY NOTES**

**14. ABSTRACT**
The main project research goals have been realised, most notably with successful 3-axis vectoring of a plasma plume using a solid state steering system consisting of concentric magnetic coils, and the creation of a tool for generating low continuous-thrust trajectories. Models have also been developed for optimal orbital trajectories within existing guidance, navigation, and weak stability boundary transfer. The outcomes demonstrate how a small spacecraft using low-thrust electric propulsion can be transferred from low Earth orbit to lunar orbit, or (via gravity assists) into interplanetary trajectories. The addition of vectoring the thrust can allow a spacecraft to maintain a fixed orientation during a maneuver. This project was led by the team at the University of Auckland (New Zealand), in collaboration with partners at L3 Harris (USA) and the Australian National University (Australia).

**15. SUBJECT TERMS**

| 16. SECURITY CLASSIFICATION OF: | | | 17. LIMITATION OF ABSTRACT | 18. NUMBER OF PAGES |
|---|---|---|---|---|
| a. REPORT<br>U | b. ABSTRACT<br>U | c. THIS PAGE<br>U | SAR | 55 |

| 19a. NAME OF RESPONSIBLE PERSON | 19b. PHONE NUMBER *(Include area code)* |
|---|---|
| GEOFFREY ANDERSEN | |

**Report Type:** Final Technical Report

**Primary contact email:** j.cater@auckland.ac.nz

**Primary contact phone:** +64 9 373 7599

**Institution Name:** The University of Auckland

**Grant Title:** Vectoring of Plasma Thrusters for CubeSats

**Grant Number:** FA2386-19-1-4012

**PI:** Dr John Cater, j.cater@auckland.ac.nz, University of Auckland, +643737599 Ext.87050

**Co-PI:** Dr Nicholas Rattenbury, n.rattenbury@auckland.ac.nz, University of Auckland, +6493737599 Ext.81224

**Co-PI:** Prof. Christine Charles, christine.charles@anu.edu.au, Australian National University, +612612 58068

**Program Officer:** Dr. Tony Kim, USAF, PhD

**Reporting Period Start Date:** 30/04/2021

**Reporting Period End Date:** 04/12/2022

**Change in Research Objectives:** There were no changes in the research objectives.

**Change in Program Officer:** Dr. Geoff Andersen <geoffrey.andersen.4@us.af.mil>

**Extensions Granted/Milestones Slipped:** 6 months extension granted due to NZ government restrictions on laboratory access during COVID19.

**Report Abstract:**

This report presents the outcomes of the project to realise a contactless magnetic thrust vectoring (MTV) system suitable for use on miniaturised propulsion systems that can be used in nanosatellites. The main project research goals have been realised, most notably with successful 3-axis vectoring of a plasma plume using a solid state steering system consisting of concentric magnetic coils, and the creation of a tool for generating low continuous-thrust trajectories. Models have also been developed for optimal orbital trajectories within existing guidance, navigation, and weak stability boundary transfer. The outcomes demonstrate how a small spacecraft using low-thrust electric propulsion can be transferred from low Earth orbit to lunar orbit, or (via gravity assists) into interplanetary trajectories. The addition of vectoring the thrust can allow a spacecraft to maintain a fixed orientation during a manoeuvre. This project was led by the team at the University of Auckland (New Zealand), in collaboration with partners at L3 Harris (USA) and the Australian National University (Australia).

**Introduction/Overview:**

This project was planned in four work packages; characterization of magnetic thrust vectoring (MTV) in simulation and experiments with a large scale thruster, miniaturisation to a CubeSat-compatible system, optimization of the MTV system and orbital trajectory planning using constant thrust and vectoring. The main outcomes of the project are described in the refereed publications attached to the report.

**Work Package 1: Plasma Characterisation**

The significant effort in WP1 focussed on the design and construction of the MTV system. This work was led by University of Auckland PhD student Antonella Caldarelli, and successful realisation of thrust vectoring was published in 2022 (Caldarelli et al. 2022a, 2022b). During the project the plasma plume experimental apparatus was constructed (Filleul et al. 2021), calibrated, and the results validated using multiple measurement techniques, which required the development of some novel approaches (Caldarelli et al. 2022c, submitted). The 3-axis coil system to enable MTV was designed and implemented as shown below in Figures 1 & 2.

**Work Package 2: Thruster Miniaturisation**

Work on miniaturising the thruster centred on the use of a high-temperature superconductor (HTS) based MTV, and was undertaken with researchers at the Robinson Research Institute, Victoria University of Wellington (New Zealand). However, while a preliminary design and simulation indicated that a suitable HTS magnet was feasible, the requirements for the power system and necessary cryocooler were out-of-scope for the project. Further research on developing an HTS system suitable for spaceflight continues with RRI as part of a research programme funded by the New Zealand Ministry of Business, Innovation & Enterprise.

**Work Package 3: MTV Optimization**

Travel to ANU for experimental thruster optimisation was prevented by COVID19 restrictions in New Zealand, however additional experimental work at UoA was conducted that resulted in a technique for achieving higher plasma densities, and thus higher thruster efficiencies (Filleul et al. 2022).

**Work Package 4: Trajectory Optimization**

Low-thrust trajectory work was led by University of Auckland PhD student Darcey Graham and in conjunction with Waqar Zaidi at L3Harris (previously ADS) and resulted in two publications (Graham et al., 2020, 2022), with further publications likely to arise in early 2023. The detailed description of the code development undertaken was presented in the previous report and optimised trajectories were found for a spacecraft using a low delta-v thruster, operating in the Earth-Moon and Earth-Venus environments. Initial trajectories found using the technique developed can be used as a starting point for higher fidelity trajectory optimization.

**Team:**

The project team consisted of the following staff; UoA: Dr John Cater, Dr Nicholas Rattenbury, UoA Graduate Students: Antonella Caldarelli, Darcey Graham, Felicien Filleul (employed as a research assistant), ANU: Prof. Christine Charles. L3 Harris staff included: Dr Thomas Kelecy and Dr Waqar Zaidi.

The team maintained and developed a relationship with Jacob Englander, interplanetary trajectory analyst formerly of NASA Goddard Space Flight Centre and now at the Applied Physics Laboratory. Cater and Rattenbury continue to work with the Robinson Research Institute at the Victoria University of Wellington on mission design for a spacecraft with a magneto-plasma-dynamic thruster.

**Budget:**

Since the previous report funds have been spent on:

(i) Consumables and measurement equipment for the plasma propulsion apparatus,

(ii) team travel to the International Electric Propulsion Conference, Boston, MA, July 2022.

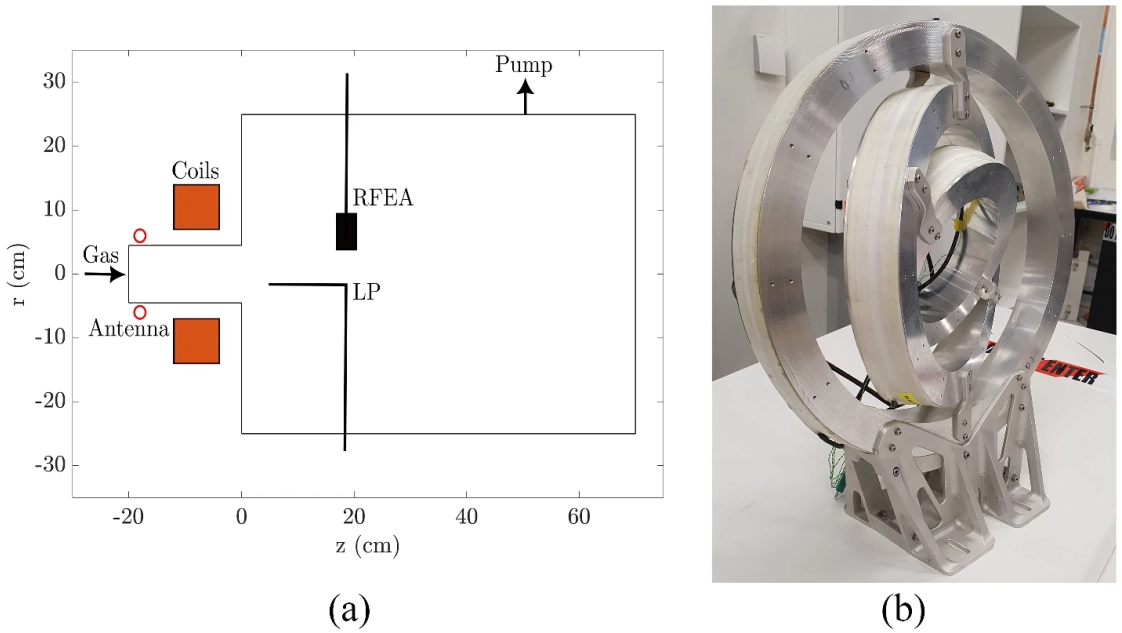


Figure 1: (a) Schematic of the experimental apparatus showing measurement devices. The plasma is energised by a small loop antenna (left). The magnetic nozzle is created by the three-axis magnetic coil system (b), shown in isolation.

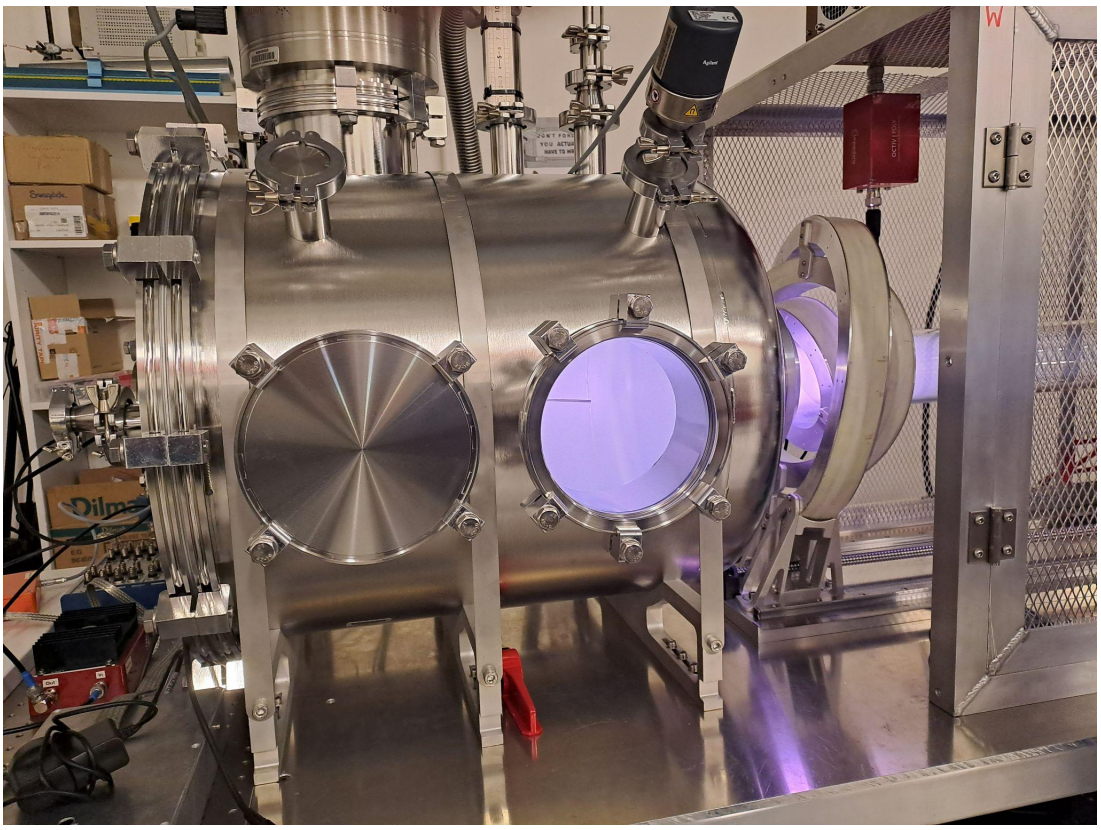

Figure 2: The plasma expansion chamber of the Huia experiment. Visible through the port in the chamber is a probe used to measure the characteristics of the plasma plume as the axial and radial direction of the ion beam is altered.

**Papers Published In Peer-Reviewed Journals (attached to report):**

Caldarelli, A., Filleul, F., Charles, C., Boswell, R., Rattenbury, N., & Cater, J. (2022). Radial characterization of an ion beam in a deflected magnetic nozzle. Journal of Electric Propulsion, 1(10).
Filleul, F., Caldarelli, A., Charles, C., Boswell, R. W., Rattenbury, N., & Cater, J. (2021). Characterization of a new variable magnetic field linear plasma device. Physics of Plasmas, 28(12), 123514.
Filleul, F., Caldarelli, A., Boswell, R., Charles, C., Rattenbury, N., & Cater, J. (2022). The role of ion magnetization on plasma generation in a magnetic nozzle RF device. Journal of Electric Propulsion, 1(20).
Graham, D. R., Englander, J. A., Rattenbury, N. J., & Cater, J. E. (2022). Low-Thrust Trajectory Design from Lunar Rideshare to Venus Capture. Journal of Spacecraft and Rockets, 1-14.

**Papers Published In Peer-Reviewed Conference Proceedings:**

Boswell, R., Filleul, F., Caldarelli, A., Charles, C., Takahashi, K., & Bennet, A. (2022). The Blue Core Paradigm. *Bulletin of the American Physical Society*.
Caldarelli, A., Filleul, F., Charles, C., Rattenbury, N., & Cater, J. (2021). Preliminary measurements of a magnetic steering system for RF plasma thruster applications. In *AIAA Propulsion and Energy 2021 Forum* (p. 3401).

Caldarelli, A., Filleul, F., Charles, C., Boswell, R., Rattenbury, N., & Cater, J. (2022b). Radial characterization of an ion beam in a deflected magnetic nozzle. In *37th International Electric Propulsion Conference*. Electric Rocket Propulsion Society, Boston.

Filleul, F., Caldarelli, A., Charles, C., Boswell, R., Rattenbury, N., & Cater, J. (2022b, June). Ion magnetization effects on plasma generation in a magnetic nozzle RF device. In *37th International Electric Propulsion Conference*. Electric Rocket Propulsion Society, Boston.

Graham, D. R., Englander, J. A., Rattenbury, N. J., & Cater, J. E. (2020, August). Low-Thrust Transfer to Interplanetary Trajectories from Lunar Trajectories with Rideshare. In *AAS/AIAA Astrodynamics Specialist Conference*.

**Publications Submitted for Peer-Review:**

Caldarelli, A., Filleul, F., Boswell, R., Charles, C., Rattenbury, N., & Cater, J. (2022c). Data Processing Techniques for Ion and Electron Energy Distribution Functions. *arXiv preprint arXiv:2211.03254*.

Journal of Electric Propulsion

RESEARCH Open Access

# Radial characterization of an ion beam in a deflected magnetic nozzle

Antonella Caldarelli[1,2*], Félicien Filleul[1,3], Christine Charles[4], Rod Boswell[4], Nicholas Rattenbury[1,3] and John Cater[1,2]

*Correspondence: antonella.caldarelli@auckland.ac.nz

[1] Te Pūnaha Ātea - Space Institute, The University of Auckland, Auckland 1010, New Zealand
[2] Department of Engineering Science, The University of Auckland, Auckland 1010, New Zealand
[3] Department of Physics, The University of Auckland, Auckland 1010, New Zealand
[4] Space Plasma, Power and Propulsion Laboratory, Research School of Physics, Australian National University, Canberra 2601, Australia

**Abstract**

The radial characterization of an ion beam generated in a magnetically steered radio-frequency (RF) plasma source is presented. In the symmetrical magnetic nozzle (MN) configuration, radial profiles of the ion saturation current obtained with a planar Langmuir probe show a double-peaked profile. The same behaviour is confirmed by the radial measurements of the total ion current and the ion energy distribution functions (IEDFs) obtained with a retarding field energy analyzer. The IEDFs also show the presence of an ion beam centred at $r = -2$ cm. On the contrary, radial measurements taken with a magnetic nozzle deflected on the $r - z$ plane exhibit a single-peaked profile with both the local ion population and the ion beam centred at $r = -5$ cm, in the direction of the MN orientation. It is shown that the ion beam location is changed as a result of a deflected magnetic nozzle, and that it follows the direction of increasing radial magnetic field.

**Keywords:** Magnetic nozzle, Ion beam, Magnetic steering, RF plasma

## Introduction

In the last decade, the aerospace industry has seen a boom in the manufacturing of small and nano-scale satellites for space communications, environmental and weather monitoring, and scientific research. The miniaturisation of spacecraft means that they are cheaper to build, cheaper to launch and provide greater flexibility when designing a space mission. However, their size poses restrictions in terms of mass, volume and power budget. Mechanical systems, such as reaction wheels, have been employed so far to control the thrust vector of the spacecraft and perform attitude and orbit control (AOC) manoeuvres. These devices are usually heavy and complex, and their movable components add potential failure modes to the mission. The concept of contactless thrust control could allow for more reliable AOC systems.

Electric propulsion (EP) systems have been extensively used in space missions given the high specific impulses that can be generated and the subsequent savings in propellant mass requirements. Contactless steering systems that employ electromagnetic fields to control the motion of charged particles have been studied in the past for Hall effect thrusters [1, 2]. Magnetic nozzle (MN) radio-frequency (RF) plasma thrusters

(sometimes referred to as Helicon thrusters) are a new electric propulsion technology which has become of interest in the last two decades as an alternative to other high power EP systems. A recent experimental campaign has shown thruster efficiencies of $\approx$ 20% and up to 70 mN of thrust for 6 kW of RF power input [3], and the generation of an accelerated ion beam caused by either a current-free double-layer or an ambipolar electric field has been demonstrated in such devices [4–7]. Due to the nature of their design, the idea of controlling the thrust vector by means of a steerable magnetic nozzle (a convergent-divergent magnetic field) has been proposed [8, 9]. Magnetic thrust vectoring would allow for a simpler and more reliable orbit and attitude control mechanism since it does not comprise of any moving/rotating components.

To assess the potential of magnetic thrust vectoring, it is important to characterize and understand the physical properties of a plasma generated and expanding in a deflected magnetic nozzle. The first experimental study of steering of an ion beam in a RF plasma thruster was done by Cox et al. [8] in the Chi-Kung reactor. Transverse magnetic fields (TMF) were applied with respect to the thruster axis, and their effect on the plasma accelerated in the electric field of a double-layer was investigated. It was noticed that the ion beam was effectively deflected as a result of the TMF. However, the magnetic field was not the dominant factor in controlling the ion beam deflection, as the latter was not following the orientation of the TMFs. Additionally, the system allowed only for magnetic steering in one plane. Merino and Ahedo [9] analysed the theoretical performance of a 3D magnetic steering system for a plasma jet. Assuming a fully magnetised ion population and a collisionless plasma, they modelled a steerable magnetic nozzle and its effect on the plasma plume. As they only presented an analytical model, no actual experimental data were discussed. Imai and Takahashi [7] measured the axial and horizontal thrust components of a MN RF plasma under an asymmetrical magnetic field. Thrust vector control by magnetic steering was experimentally demonstrated in two dimensions by mounting four additional solenoids after the plasma source exit by Takahashi & Imai [10]. Spatial mapping of the ion saturation current showed that the plasma plume was effectively being deflected, and that the plasma density profile was following the magnetic nozzle orientation, but the experiments lacked the characterization of an ion beam in the steered configuration. Due to the location of the thrust vector control system, the implementation of their design in an actual thruster would also not be trivial.

The aim of this study is to present the first measurements of a novel magnetic steering system based on the study by [9] incorporated into a radio-frequency plasma reactor at The University of Auckland. The aim of the research is to study how the characteristics of an expanding plasma are affected by different magnetic nozzle orientations, with particular focus on the generation of an accelerated ion beam. As such, it is out of the scope of the project to directly measure the thrust components and quantify the thrust vector capability of the system. Radial profiles of an argon plasma expanding in a magnetic nozzle deflected on the *r-z* plane are presented. Specifically, a retarding field energy analyzer was used to radially characterize the ion energy distribution function, and measurements of a deflected ion beam are presented. Radial profiles of the ion saturation current taken with a planar Langmuir probe are also discussed to qualitatively assess the plasma deflection expanding in an asymmetric magnetic field.

Experimental apparatus section briefly describes the experimental apparatus and the plasma diagnostics used. Magnetic nozzle deflections section presents the magnetic nozzle characteristics from magnetostatic simulations where the magnetic steering system was modelled. Finally, Results section discusses the experimental results.

## Experimental apparatus

The experimental campaign to assess the performance of the magnetic steering system is performed in the apparatus *Moa*. The set-up is an expansion of *Huia*, a RF plasma reactor at The University of Auckland [11]. Figure 1a shows a sketch of the system with the key components. The plasma source region is defined by a 90 mm inner diameter borosilocate glass tube extended by a 500 mm diameter, 700 mm long stainless steel vacuum chamber to allow plasma expansion. *Moa* is pumped down to a base pressure $\approx 2 \times 10^{-7}$ Torr via a turbo pump with a pumping speed capability of 625 L/s for argon. During the experiments, the flow rate of gas is kept at 12 sccm to maintain a chamber pressure of 0.5 mTorr. The plasma is created by a 1.3 turns loop antenna matched via an L-type matching network to maximise power transfer from a variable frequency 1 kW RF power supply with a frequency range between 27.12 and 40.68 MHz. The antenna is made of a 3 mm diameter copper wire that was wound around a cylinder with an external diameter of 10 cm to fit around the glass tube. The point on axis at the intersection between the end of the plasma source tube and the beginning of the vacuum chamber is set as the origin of the coordinate system used throughout this study, i.e. $(r, z) = (0, 0)$ cm.

The magnetic steering system, shown in Fig. 1b, is formed by three skewed, concentric coils of increasing diameter placed co-axially with respect to the plasma source, inclined at 15° with respect to the system axis $z$ and precessed by an angle of 120° with respect to each other to create a rotational-symmetry arrangement. The three coils form the MTV system and the deflection of the magnetic nozzle is accomplished by independently

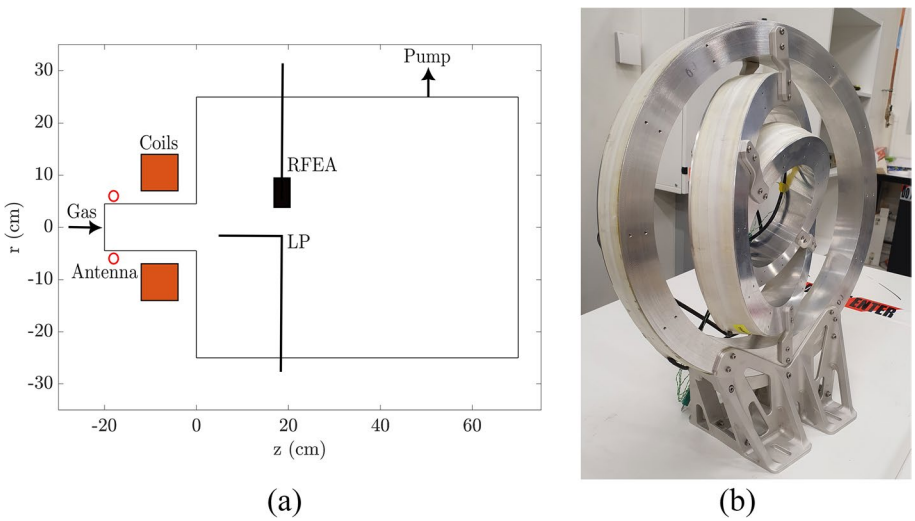


**Fig. 1** **a** Schematic of the experimental apparatus. The loop antenna is placed at $z = -18$ cm, while the centre of the magnetic steering coils is at $z = -8$ cm. **b** Picture of the magnetic steering coils

varying the current input in each coil. The design of the magnetic system is based on the study presented by [9]. The steering system is mounted at the interface between the plasma source and the vacuum chamber to steer the MN at the beginning of plasma expansion. For the purpose of this study, only the most inner coil was employed to generate the non-symmetric magnetic field and allow the magnetic nozzle to deflect on the *r-z* plane. The solenoid has an inner diameter of 70 mm, and a width of 40 mm to accommodate for 323 turns of AWG 12 copper wire.

#### Plasma diagnostics

Two main diagnostics probes were used to characterise the plasma expanding in the symmetric and deflected magnetic nozzle cases. A planar Langmuir probe (LP) was used to measure the ion saturation current, while a retarding field energy analyser (RFEA) was used to measure the plasma potential and the ion energy distribution functions. The probes were mounted on a movable (rotation and translation) 1/4" steel shaft introduced in the top ports of the expansion chamber. Both probes were moved radially in the region $-15 < r < 15$ cm.

The radial mapping of the ion saturation current $I_{\text{sat}}$ in *Moa* is used to detect steering of the plasma within the region of the deflected MN. The measurements are obtained with a Langmuir probe made out of a single sided 2 mm diameter nickel disk biased at -100 V to ensure total electron rejection. Radial profiles of $I_{\text{sat}}$ were taken with the probe placed at two different axial locations: $z_{\text{P}} = 9$ cm and $z_{\text{P}} = 19$ cm.

The design of the retarding field energy analyser used for this study is based on Ref. [12], whose similar design was also used in other studies [5, 8, 13]. The description of the RFEA and its electric circuit used herein are presented in details in Ref. [14]. It includes four mesh grids (earth, repeller, discriminator, and secondary grid) and one nickel collector plate where the ion current is measured. The aperture of the probe orifice has a diameter of 2 mm, and the grids are electrically insulated using a 0.1 mm thick polyimide sheet. The probe is operated in ion collection mode. The earth grid is grounded to ensure a uniform potential profile at the probe entrance, while the repeller grid is biased at −90V to reject all incoming electrons. The voltage of the discriminator grid is swept from 0 V to 80 V to obtain the *I-V* characteristics. The IEDFs presented in the paper were obtained from the raw *I-V* characteristics by using a Gaussian deconvolution method [4, 7].

### Magnetic nozzle deflections

The magnetic steering system was modelled on ANSYS Electronics Desktop 2021-R1 and the magnetic field was computed using the software's 3D magnetostatic solver. The symmetric magnetic nozzle configuration involved using all three coils to generate a maximum magnetic field on axis of $B_{z,\text{max}} = 320$ G. For the preliminary study of magnetic steering, only the most inner coil, MTV1, was used to deflect the magnetic nozzle on the *r-z* plane and to also produce a $B_{z,\text{max}} = 320$ G. Figure 2a and b show the magnetic field lines and the field magnitude for the symmetric and deflected case, respectively. Along the $z$ axis, the magnetic field exhibits a single peak at the magnetic nozzle throat $(r, z) = (0, -8)$ cm and it then decreases rapidly to 67 G for the symmetric case, and to 26 G for the asymmetric field case. The deflection angle of the magnetic nozzle,

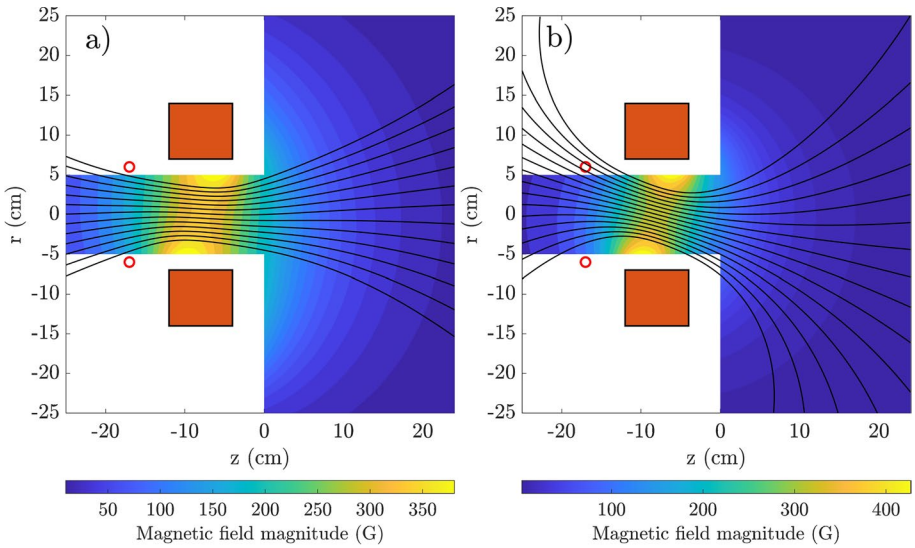


**Fig. 2** Magnetic field lines and field magnitude on the $z - r$ plane for (**a**) the symmetric magnetic nozzle case, and (**b**) the deflected magnetic nozzle case

$\theta_{\text{def}}$, was defined as the angle between the axis $z$ and the central field line with vertex at the nozzle throat i.e., $z = -8$ cm. Magnetostatic simulations predicted deflections of the magnetic nozzle of up to $\theta_{\text{def}} = \pm 14°$. The achievable MN orientations would be sufficient to perform attitude and orbit control manoeuvres as the majority of thrust vectoring corrections do not exceed 8-10°[9].

A preliminary analysis of the ion gyroradius on axis, $r_{\text{g,i}}$, was also carried out to estimate the coupling between the ions and the magnetic field. Ions are assumed to be magnetized when the ratio of their Larmor radius $r_{\text{g,i}}$ to the characteristics length of system $R$ is $r_{\text{g,i}}/R < 1$. Considering ions with a thermal speed of approximately 400 m/s and at room temperature [15, 16], the ions are assumed to be well magnetised in the plasma source for both the symmetric and the deflected nozzle orientation ($r_{\text{g,i}}/R \ll 1$), where the characteristic length of the system is the glass tube radius i.e., $R = 4.5$ cm. In such a configuration (i.e. axial location of MN throat and antenna not coinciding), it has been shown that an increase in axial plasma density in the source is achieved when the ions are magnetized under the antenna [11, 15, 17]. In the expansion chamber, where the characteristic length of the system is the expansion chamber radius, where $R = 25$ cm, for the symmetric case, the ions are magnetized in the region of interest for the measurements ($r_{\text{g,i}}/R < 1$). In the asymmetric magnetic field case, the ion gyroradius on axis becomes comparable to the chamber radius at a distance of 19 cm from the source exit ($r_{\text{g,i}}/R \approx 1$), leading to a partially-magnetized ion population in the $z_{\text{p}} = 19$ cm measurements region.

## Results

Radial measurements of the plasma were initially done in a symmetrical magnetic nozzle configuration to obtain a baseline profile of the plasma. For this study, the experiments were carried out at a frequency of 27.12 MHz, an RF power of 250 W, an argon pressure of 0.5 mTorr, and a $B_{z,\text{max}}$ of 320 G for both the symmetric and deflected magnetic

nozzle case. Given that the frequency used does not affect the overall plasma characteristics and behaviour [11], conducting the experiments at 27.12 MHz would have not resulted in any substantial difference than if they were run at the standard 13.56 MHz. During the data acquisition, the plasma remained stable with a reflected power always less than 0.5%.

#### Ion saturation current profiles

Figure 3a and b show the radial profiles of the ion saturation current measured with the Langmuir probe at $z_P = 9$ cm and $z_P = 19$ cm for the symmetric and deflected MN orientation, respectively.

For the symmetric case, $I_{sat}$ exhibits a peak at $r = -7$ cm and one at $r = 5$ cm when the LP is located at $z_P = 9$ cm. When the data is collected at $z_P = 19$ cm, the ion saturation current peaks are at $r = -10$ cm and at $r = 8$ cm. Measurements of $I_{sat}$ taken in the plasma source showed a single maximum on axis, implying that the double-peaked current profile occurs downstream in the diverging magnetic nozzle section. This feature has been reported in other RF devices when the plasma has been expanding in a magnetic nozzle [7, 18–20]. The formation of these high density conics has been attributed to hot electrons generated under the antenna that escape the plasma source along the last radial field lines leaving the glass tube [19–21]. Additionally, it has been shown that the generated thrust in a magnetic nozzle RF thruster is increased by this high electron pressure conical structure [22]. It is also worth noticing that the plasma presents an asymmetric radial profile even for the symmetric magnetic nozzle configuration. This asymmetry could be due to a non-uniform power deposition and subsequent plasma generation process in the source [7, 23]. The highest RF voltage drop occurring between the two antenna ends could lead to capacitive coupling happening under this region.

The ion saturation current profile for the deflected MN case (Fig. 3b) presents a very different trend. $I_{sat}$ shows a single peak centred at $r = -4$ cm for $z_P = 9$ cm, and at $r = -5$ cm for $z_P = 19$ cm. A possible cause of the double-peak to single-peak profile

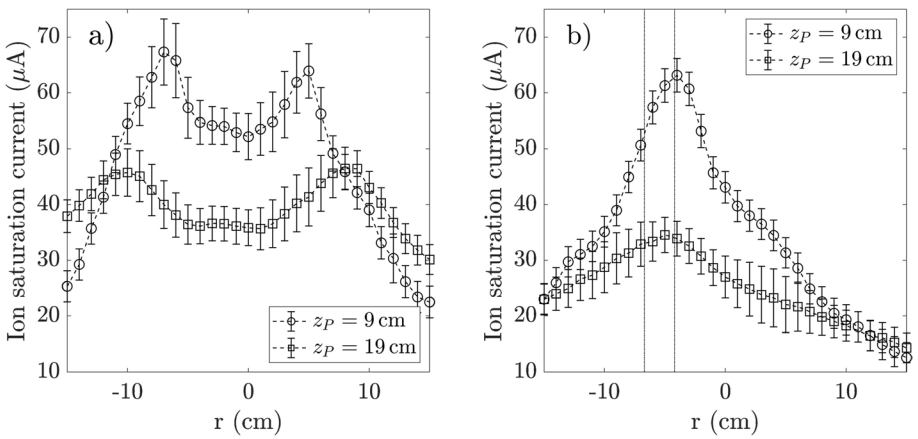


**Fig. 3** Radial profiles of the ion saturation current taken with the Langmuir probe at $z_P = 9$ cm (open circles) and $z_P = 19$ cm (open squares) for: (**a**) the symmetric magnetic nozzle case, and (**b**) the deflected magnetic nozzle case. The sampling rate of the data acquisition unit was set to $10^5$Sample/s, where each scan lasted 1 s. At each location, the reported $I_{sat}$ is the average of $10^5$ samples. The vertical dash-dotted lines in (**b**) represent the radial location of the central magnetic field line at $z = 9$ cm and $z = 19$ cm

transition in the deflected magnetic nozzle case could be the non-uniformity of the magnetic field in the plasma source (which is clear in Fig. 2b). Some of the high energy electrons created under the antenna will be lost to the source walls following the bent streamlines thereby inhibiting their escape from the plasma source into the chamber and reducing local ionization downstream of the MN. The drop in the collected $I_{sat}$ when compared to the symmetric case could be caused by an increased plasma loss to the source wall before expanding in the chamber, following the deflected field lines. When analysing the radial profiles, it is interesting to consider the direction of the central magnetic field line. At $z = 9$ cm, the central magnetic field line deflected by $\theta_{def} = 14°$ has a radial coordinate of $r = -4.2$ cm, which coincides with the peak in current measured at $(r - z) = (-4, 9)$ cm. On the other hand, the radial position of the deflected central field line at $z = 19$ cm would be $-6.7$ cm, while the $I_{sat}$ peak is measured at $(r - z) = (-5, 19)$ cm. This discrepancy could be explained by ion demagnetization, and the subsequent ion detachment from the field lines, at $z = 19$ cm where the calculated gyroradius of the thermal ions is comparable to the chamber radius.

#### Ion beam detection

For thruster applications, the existence of an accelerated ion population is a key contribution to the axial momentum flux exhausted from the source i.e., the axial force [22]. In the current experimental set up, ion-neutral collisions affect the accelerated ion population expanding in the magnetic nozzle, where charge-exchange collisions create slow ions and fast neutrals. Thus, the ion beam component decreases and the measured thermal ion population increases. The formation of the high-density conics in the symmetric MN case have also been linked to downstream ionization that would add to the local ion population [18]. At the operating conditions of this study, the presence of an ion beam can be detected by an RFEA and it is characterised by a second peak in the IEDF at a higher voltage than the plasma potential, where the beam potential, $V_B$, is defined as the location of this second maximum. To ensure that the RFEA was actually measuring an accelerated ion population, the ion energy distribution functions measured at the same experimental

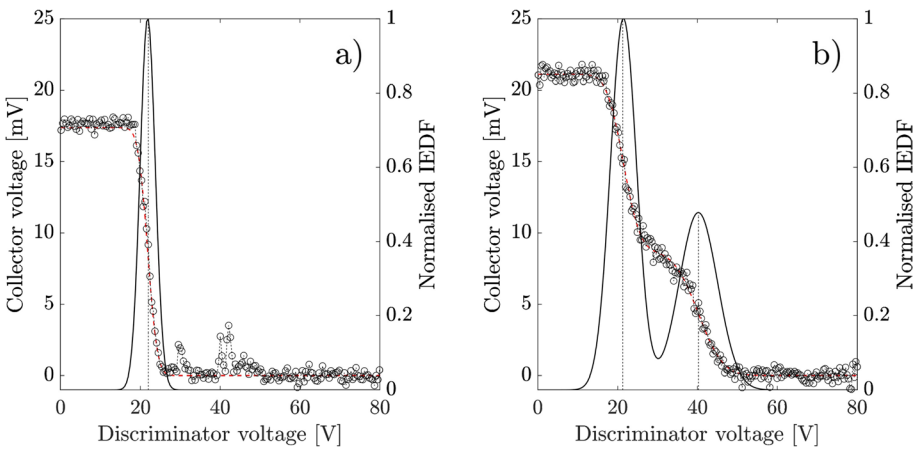


**Fig. 4** I-V characteristics measured with the RFEA at $(r, z) = (0, 19)$ cm at $P_{RF} = 250$ W, $B_{z,max} = 320$ G in a symmetric MN configuration, and 0.5 mTorr. **a** Radial-facing RFEA, $V_P = 21.98$ V (**b**) Source-facing RFEA, $V_P = 21.28$ V and $V_B = 40.25$ V

condition but with the probe orifice first facing the chamber walls (radial-facing) and then facing the plasma source exit (source-facing) were compared. Figure 4 shows the *I-V* characteristics and the derived IEDFs for both the radial-facing and source-facing RFEA orientation. The radial-facing profile shows one peak located at a plasma potential of $V_P = 21.98$ V. On the other hand, the IEDF obtained from the source-facing RFEA presents two peaks: one at the local plasma potential $V_P = 21.28$ V, and the second one at a higher potential, $V_B = 40.25$ V. Because of the extreme similarity between the measured plasma potentials, one can infer that the IEDF does not present a distribution broadening effect, nor that the probe orientation is significantly perturbing the plasma, but that the RFEA is actually measuring a higher energetic, directional ion beam [4, 12, 13].

#### Ion beam characterization

The retarding field energy analyzer is used to radially characterize the ion energy distribution function, the total ion current, and the plasma and ion beam potentials. The probe is placed at $z_P = 19$ cm and with the orifice facing the plasma source exit to collect the ion beam signal. The standard deviation of the measured current is calculated to be $0.2\mu$A. For the symmetric case, the total ion current plot in Fig. 5 shows a double-peaked, slightly asymmetric profile confirming the ion saturation current profile measured by the Langmuir probe. Indeed, the $I_0$ plot presents a maximum at $r = -11$ cm and at $r = 8$ cm. Contrarily, the deflected MN case shows a single peak centred at $r = -5$ cm, again similar to the $I_{sat}$ profile of Fig. 3a.

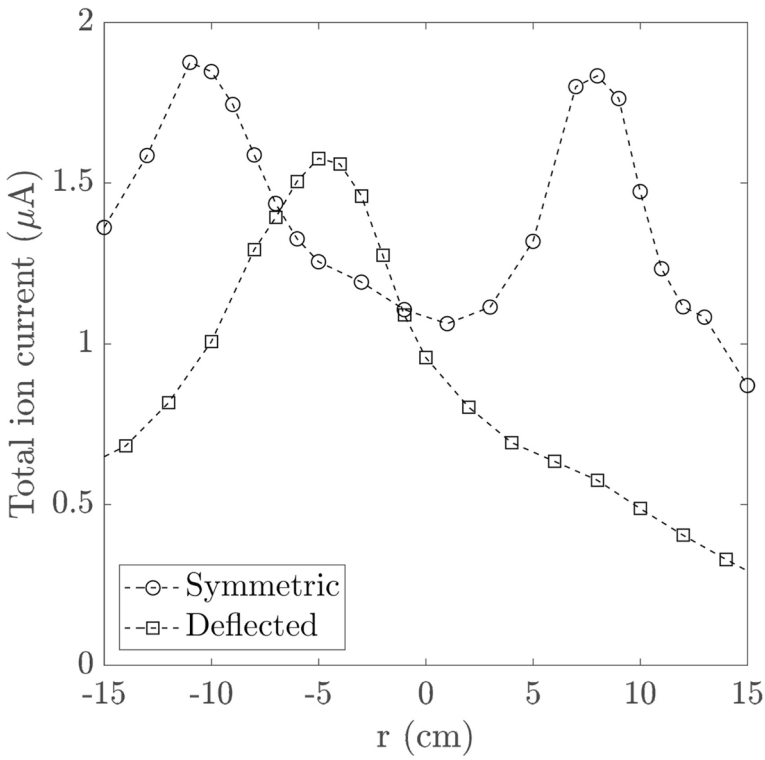


**Fig. 5** Radial profiles of the total ion current measured by the RFEA at $z_P = 19$ cm for the symmetric magnetic nozzle case (open circles) and the deflected MN case (open squares)

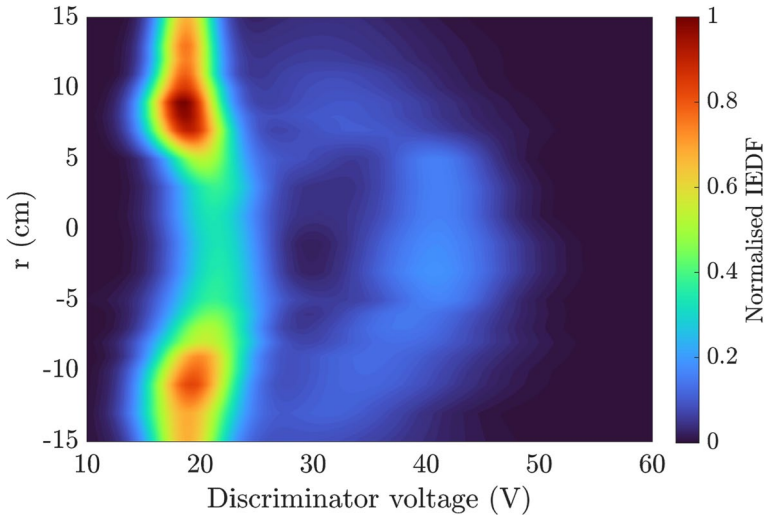


**Fig. 6** Ion energy distribution functions as a function of radial position and discriminator voltage taken with the RFEA at $z = 19$ cm for the symmetric magnetic nozzle case

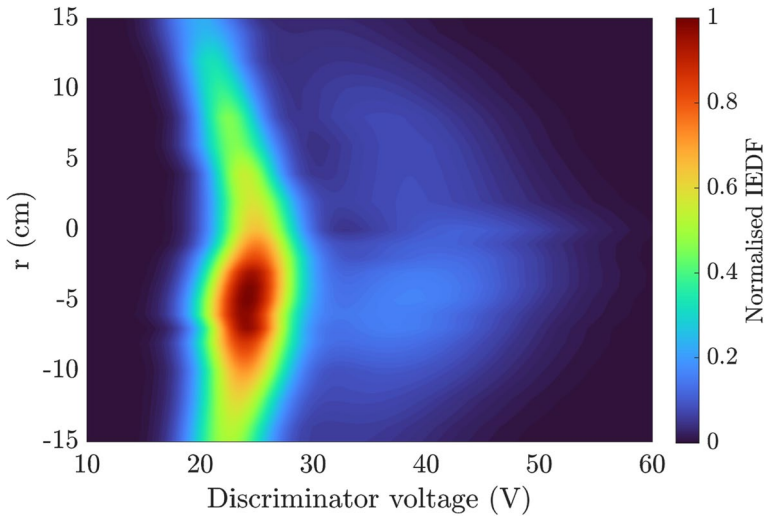


**Fig. 7** Ion energy distribution functions as a function of radial position and discriminator voltage taken with the RFEA at $z = 19$ cm for the deflected magnetic nozzle case

Figure 6 shows the contour plots of the normalised ion energy distribution functions as a function of radial position and potential for the symmetric magnetic nozzle case. The IEDFs show a local thermal population of ions at $V_P \approx 20$ V with a double-peaked profile at $r = -11$ cm and $r = 8$ cm, consistent with the measured total ion current. The energy distributions show the presence of a second, higher energetic ion population at a potential of $V_B \approx 40$ V. This accelerated population is defined as the ion beam, and it appears centred at $r = -2$ cm. An estimate of the ion beam energy at the location of its centre i.e., $(r, z) = (-2, 19)$ cm can be found as $\varepsilon_B = e(V_B - V_P) \sim 19$ eV. The ion beam potential is constant between $-5 < r < 5$ cm, and then decreases by 10 V at the edges.

The measurements taken with the asymmetric magnetic nozzle orientation clearly show the deflection of the ion beam in the direction of increasing radial magnetic field. As seen in Fig. 7, the local ion population presents a single peak at $r = -5$ cm at a slightly higher potential than the symmetric case i.e., $V_P \approx 24$ V. The energy distribution of the ion beam is not centred anymore, but it shows a shifted profile that also peaks at $r = -5$ cm, and it is characterised by a narrower beam width. Additionally, the potential of the accelerated ions peaks at $r = 0$ cm where $V_B \approx 43$ V to then decrease radially e.g., $V_B \approx 38$ V at $r = -5$ cm. The energy of the ion beam in the deflected case at $(r, z) = (-5, 19)$ cm is then estimated to be $\varepsilon_B \sim 14$ eV. It is noticed that the ion-neutral mean free path for the operating pressure is shorter than the distance between the source exit and the probe position i.e., $\lambda_{mfp} \sim 10$ cm and $z_P = 19$ cm. Thus, the accelerated ion beam component is decreased at the measurement location due to charge-exchange collisions, and elastic collisions could affect its direction, further reducing the collected beam current. Additionally, the plasma profile structure for both the symmetric and deflected magnetic nozzle scenario peaks in the centre and decreases radially, indicating the presence of an electric field that would accelerate the ions outwards increasing the plasma cross-field diffusion.

## Conclusion

The first measurements of a magnetic steering system mounted co-axially in a magnetic nozzle radio-frequency plasma thruster at The University of Auckland are presented. A Langmuir probe and a retarding field energy analyzer were used to radially characterize the plasma expansion in a symmetric and deflected magnetic nozzle. In the symmetric configuration, both the ion saturation current and the ion energy distribution radial profiles showed a double-peaked behaviour. The latter could be a sign of high density conics formation and local ionization downstream of the plasma source caused by transport of hot electrons from the antenna region. The measurements taken in the deflected magnetic nozzle case proved that the plasma was affected by the asymmetric magnetic field. Radial profiles of the ion saturation current, the total ion current and of the IEDFs changed from a double-peaked to a single peak profile centred around $r = -5$ cm in the direction of the magnetic nozzle. However, further experiments are required to fully understand the generation of the high-density conics, and how to optimize the magnetic steering system to allow for the conics to be created even when the magnetic nozzle is deflected.

The ion energy distribution functions clearly showed the radial location of the ion beam changing with the deflected magnetic field. The direction of the accelerated ion beam was found to be following the magnetic nozzle orientation, even though the ion beam intensity and its direction were affected by ion-neutral collisions and ion demagnetization; thus, further measurements of the ion energy distribution functions closer to the plasma source exit are necessary to quantify and better characterize the steering of an ion beam.

**Authors' contributions**

A.C. run the experiments, acquired the data and redacted the manuscript. F.F. helped in the data acquisition and the construction of the apparatus. C.C. and R.B. provided guidance in experimental RF plasmas and diagnostics. J.C. and N.R. are doctoral supervisors of A.C. and F.F. All authors reviewed the manuscript. The author(s) read and approved the final manuscript.

**Funding**
The research is being funded by the Asian Office of Aerospace Research and Development (AOARD), the international office of the Air Force Office of Scientific Research (AFOSR), under grant number #FA2386-19-1-4012.

**Availability of data and materials**
The data that support the findings of this study are available from the corresponding author upon reasonable request.

## Declarations

**Competing interests**
The authors declare that they have no competing interests.

Received: 4 August 2022 Accepted: 7 September 2022
Published online: 14 September 2022

**References**

1. Duchemin O, Prioul M, Illand H, Banetta S, Vicini A, Garrigues L et al (2004) Development of a prototype thrust steering device for hall-effect thrusters. In: Wilson A (ed) 4th International Spacecraft Propulsion Conference, vol. 555. ESA Special Publication, Cagliari, p 42–1. https://ui.adsabs.harvard.edu/abs/2004ESASP.555E..42D
2. Garrigues L, Boniface C, Hagelaar GJM et al (2009) Performance modeling of a thrust vectoring device for hall effect thrusters. J Propuls Power 25(5):1003–1012. https://doi.org/10.2514/1.39680
3. Takahashi K (2021) Magnetic nozzle radiofrequency plasma thruster approaching twenty percent thruster efficiency. Sci Rep 11:2768. https://doi.org/10.1038/s41598-021-82471-2
4. Charles C, Boswell R (2004) Laboratory evidence of a supersonic ion beam generated by a current-free "helicon" double-layer. Phys Plasmas 11(4):1706–1714. https://doi.org/10.1063/1.1652058
5. Bennet A, Charles C, Boswell R (2018) In situ electrostatic characterisation of ion beams in the region of ion acceleration. Phys Plasmas 25(2):023516. https://doi.org/10.1063/1.5017049
6. Takahashi K (2019) Helicon-type radiofrequency plasma thrusters and magnetic plasma nozzles. Rev Mod Plasma Phys 3:044510. https://doi.org/10.1007/s41614-019-0024-2
7. Imai R, Takahashi K (2022) Deflections of dynamic momentum flux and electron diamagnetic thrust in a magnetically steered rf plasma thruster. J Phys D Appl Phys 55(13):135201. https://doi.org/10.1088/1361-6463/ac4451
8. Cox W, Charles C, Boswell RW et al (2010) Magnetic ion beam deflection in the helicon double-layer thruster. J Propuls Power 26(5):1045–1052. https://doi.org/10.2514/1.49202
9. Merino M, Ahedo E (2017) Contactless steering of a plasma jet with a 3d magnetic nozzle. Plasma Sources Sci Technol 26:095001. https://doi.org/10.1088/1361-6595/aa8061
10. Takahashi K, Imai R (2022) Two-dimensional deflection of a plasma plume exhausted from a magnetically steered radiofrequency plasma thruster. Phys Plasmas 29(5):054501. https://doi.org/10.1063/5.0090476
11. Filleul F, Caldarelli A, Charles C et al (2021) Characterization of a new variable magnetic field linear plasma device. Phys Plasmas 28(12):123514. https://doi.org/10.1063/5.0070924
12. Conway GD, Perry AJ, Boswell RW (1998) Evolution of ion and electron energy distributions in pulsed helicon plasma discharges. Plasma Sources Sci Technol 7(3):337–347. https://doi.org/10.1088/0963-0252/7/3/012
13. Charles C, Degeling AW, Sheridan TE et al (2000) Absolute measurements and modeling of radio frequency electric fields using a retarding field energy analyzer. Phys Plasmas 7(12):5232–5241. https://doi.org/10.1063/1.1322557
14. Caldarelli A, Filleul F, Charles C et al (2021) Preliminary Measurements of a Magnetic Steering System for RF Plasma Thruster Applications. In: AIAA Propulsion and Energy 2021 Forum, p 3401. https://doi.org/10.2514/6.2021-3401
15. Bennet A, Charles C, Boswell R (2019) Non-local plasma generation in a magnetic nozzle. Phys Plasmas 26(7):072107. https://doi.org/10.1063/1.5098484
16. Chabert P, Braithwaite N (2011) Physics of Radio-Frequency Plasmas. Cambridge University Press. https://doi.org/10.1017/CBO9780511974342
17. Filleul F, Caldarelli A, Charles C et al (2022) Ion magnetization effects on plasma generation in a magnetic nozzle RF device. In: 37th International Electric Propulsion Conference. Electric Rocket Propulsion Society, Boston
18. Charles C (2010) High density conics in a magnetically expanding helicon plasma. Appl Phys Lett 96(5):051502. https://doi.org/10.1063/1.3309668
19. Takahashi K, Akahoshi H, Charles C et al (2017) High temperature electrons exhausted from rf plasma sources along a magnetic nozzle. Phys Plasmas 24(8):084503. https://doi.org/10.1063/1.4990110
20. Bennet A, Charles C, Boswell R (2018) Selective radial release of hot, magnetised electrons downstream of a low-pressure expanding plasma. J Phys D Appl Phys 51(37):375204. https://doi.org/10.1088/1361-6463/aad74f
21. Yadav S, Ghosh S, Bose S et al (2018) Role of ion magnetization in formation of radial density profile in magnetically expanding plasma produced by helicon antenna. Phys Plasmas 25(4):043518. https://doi.org/10.1063/1.5028576
22. Takahashi K, Sugawara T, Ando A (2020) Spatial measurement of axial and radial momentum fluxes of a plasma expanding in a magnetic nozzle. New J Phys 22(7):073034. https://doi.org/10.1088/1367-2630/ab98d5
23. Gulbrandsen N, Fredriksen A (2017) Rfea measurements of high-energy electrons in a helicon plasma device with expanding magnetic field. Front Phys 5. https://doi.org/10.3389/fphy.2017.00002

## Publisher's Note

Journal of Electric Propulsion

RESEARCH Open Access

# The role of ion magnetization on plasma generation in a magnetic nozzle rf device

Félicien Filleul[1,2,3*], Antonella Caldarelli[2,3], Rod Boswell[4], Christine Charles[4], Nicholas Rattenbury[1,3] and John Cater[2,3]

*Correspondence:
felicien.filleul@auckland.ac.nz

[1] Department of Physics, The University of Auckland, Auckland 1010, New Zealand
[2] Department of Engineering Science, The University of Auckland, Auckland 1010, New Zealand
[3] Te Pūnaha Ātea - Space Institute, The University of Auckland, Auckland 1010, New Zealand
[4] Space Plasma, Power and Propulsion Laboratory, Research School of Physics, The Australian National University, Canberra ACT 2601, Australia

**Abstract**

Two dimensional mappings of the floating potential, Ar II emission and ion saturation currents are used to characterize an 80 cm long magnetized rf plasma column. The data brings new evidence supporting that the level of ion magnetization under the rf loop antenna plays an important role for the efficient generation of plasma over an extended region when the magnetic nozzle is sufficiently separated from the antenna. Densities up to $10^{18}$ $m^{-3}$ and a blue core are observed for an rf power of 200 W and magnetic fields above 400 G when ions are magnetized. The local wall charging under the antenna is probed and observed to change coherently with the local ion magnetization and seems critical to the global creation and transport of energetic electrons, which are indirectly observed far from the antenna when the ion Larmor radius is much smaller than the glass tube radius over the entire region of investigation.

**Keywords:** Magnetic nozzle, Anisotropic charging, Blue core, Electron transport

## Introduction

Spontaneous acceleration of quasineutral plasmas through a magnetic nozzle (MN) is one of the basic principles of novel spacecraft electric propulsion [1, 2]. One such propulsion technology, the helicon thruster (HT), also called magnetic nozzle rf plasma thruster, has been continuously scrutinized both theoretically and experimentally over the past 20 years. This has recently resulted in the milestone of a prototype achieving a thrust of $\sim 55$ mN and an efficiency of nearly 20% at 4 kW using argon [3]. Efforts are on-going to further improve the understanding of the thrust generation mechanisms and increase the system efficiency in order to make HT competitive with legacy thruster technologies [2]. The motivation comes from the HT promises of longer lifetime and system simplicity, thanks to having no electrode or live elements in contact with the plasma [4].

Several mechanisms contributing to the thrust generation have been identified since the first report of an ion beam-generating current-free double layer in a helicon device in 2003 [4]. From the force balance point of view, the total thrust has two principal positive contributions. The first one is the thermal plasma pressure on the backplate of the thruster source tube. The second one is a Lorentz force owing to an azimuthal

diamagnetic electron drift interacting with the radial component of the applied magnetic field [5]. Diamagnetic drifts are induced by radial gradients in electron pressure and tailoring the radial profiles of electron density and temperature is therefore key to achieving a high performing thruster. In particular, peripheral high density and high temperature conical structures have been repeatedly observed downstream of a MN [6–8]. Studies have quantified the contribution of these structures to the axial momentum flux, while their geometry would result in a larger plume divergence compared to axially peaked plasma structures [9, 10]. The leading hypothesis for the formation of high density conics is local ionization by electrons energized a few skin depths under the rf antenna and exiting along some of the most radially outward magnetic streamlines capable of escaping the thruster source [6, 7, 11]. A good understanding of the efficient transport of energetic particles is therefore key.

Radial ion fluxes and associated momentum loss to the radial source wall have been identified as affecting the HT's efficiency [12, 13]. Increasing the magnetic field intensity can reduce the cross-field diffusion and studies have found the level of ion magnetization in the source tube to be a critical parameter in obtaining an ion beam [13–17]. Recent studies have correlated the level of ion magnetization in the source tube with the observations of plasma densities $\geq 10^{18}$ m$^{-3}$ at the MN throat, for relatively low rf powers and magnetic field intensities [18–20]. In a similar fashion to the conics, this high density peak at the location of strongest axial magnetic field seems to be predominantly due to remote ionization by energetic electrons transported from the antenna region, while a wave-heated regime has not been identified so far for such configurations [19]. For efficient transport of these high energy electrons, the anisotropic charging of the dielectric source tube could be an important factor [19, 20]. The magnetic behavior of the plasma in the source tube is therefore another key factor to consider for improving the performances of the MN rf thruster. Localized charging under the rf antenna due to an asymmetrical capacitive mode is also anticipated to pay a role in the ion dynamics [21].

This study presents evidence of the role of ion magnetization and associated ion-wall interactions in the generation of high density plasmas in the region from the rf antenna to the MN at a relatively low rf power of 200 W. The hypothesis of ion magnetization-driven local wall charging affecting the transport of hot electrons is investigated through local and volumetric ion saturation and floating potential measurements. The in-situ measurements are completed by nondisruptive optical emission intensity diagnostics. The findings are discussed in terms of their expected impacts on magnetic nozzle rf thruster performances. Section 2 presents the apparatus and employed diagnostics, Section 3 briefly reviews the two modes of operation of the plasma discharge, and Section 4 details the volumetric and glass tube surface floating potentials. Section 5 relates the findings to the efficient generation of high plasma densities.

## Apparatus & diagnostics

The measurements are conducted in *Huia*, a plasma experiment at the University of Auckland specifically designed to allow flexible study of rf magnetized plasma generation and transport. *Huia*'s active plasma region is a 150 cm long, 9 cm inner diameter borosilicate glass tube, a section of which is represented in Fig. 1. *Huia* is complementary to the Australian National University based *Echidna* experiment, working at different

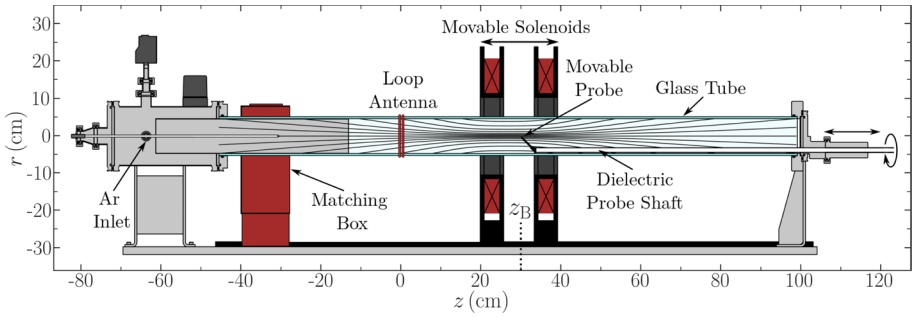


**Fig. 1** Schematic of the *Huia* plasma device with main components labeled. The loop antenna is located at $z = 0$ cm while the movable solenoid pair is centered at $z = z_B = 30$ cm. The movable planar Langmuir probe is inserted through a linear/rotary vacuum feedthrough at $z = 120$ cm. The axial location of the gas inlet coincides with the axial location of the turbo pump inlet. The light grey elements are all grounded

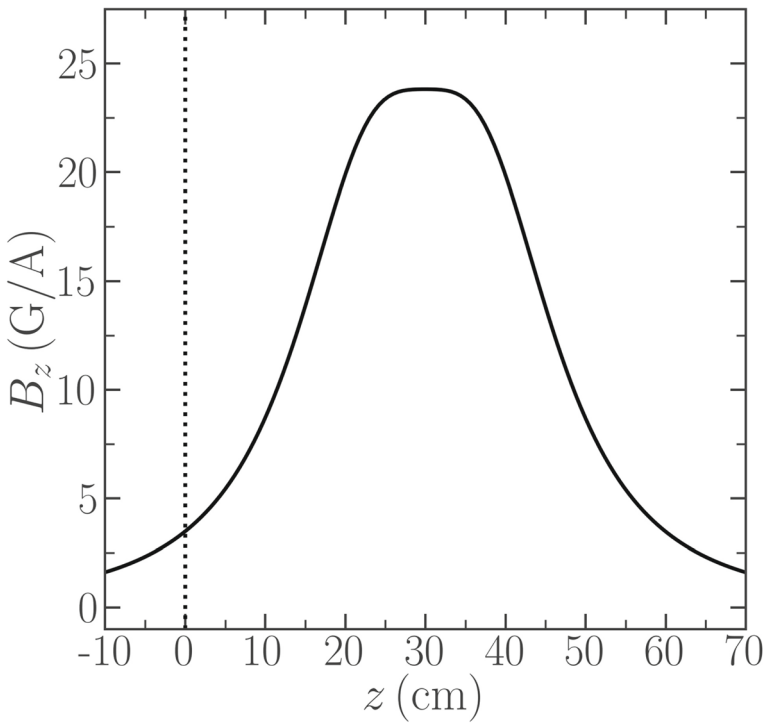


**Fig. 2** Axial magnetic flux density with the solenoids placed at $z_B = 30$ cm. The dotted vertical line marks the position of the loop antenna

radiofrequencies and using a different rf antenna type [19]. A base pressure of a few $10^{-7}$ Torr is maintained with a 250 l/s turbo pump backed by a primary pump. Argon is injected upstream of the glass tube through a mass-flow controller. The power from a 1 kW rf generator set at 27.12 MHz is fed to a 4/3 turn tightly wound loop antenna, the center of which marks the origin of *Huia*'s $(r, z)$ reference frame (see Fig. 1). The rf load impedance is matched to 50 Ω using an L-type matching network. A pair of solenoids of 352 turns each is used in a Helmholtz configuration to create a maximum magnetic flux density of 23.82 G/A on axis. The axial magnetic flux density profile is shown in Fig. 2. The position of the solenoids can be adjusted from $z = -10$ cm to $z = 80$ cm, allowing a

wide range of magnetic field configurations. The axial position of the center of the solenoids is denoted as $z_B$, which also marks the location of maximum axial magnetic field intensity $B_0$.

In the results that follow, the rf power was maintained at 200 W with a reflected power smaller than 1% at all times. The argon pressure is fixed at 1 mTorr and the antenna-solenoids distance was varied between $z_B = 0$ cm and 40 cm. The maximum axial magnetic flux density is varied between 75 G to 950 G.

The plasma floating potential $V_f$ and the ion saturation current $I_{sat}$ are measured using a 2 mm diameter nickel disk mounted atop a thin ceramic tube to form an uncompensated planar Langmuir probe (LP). The probe is left floating to acquire $V_f$ or is biased at −100 V to measure $I_{sat}$ [22]. Where the electron temperature $T_e$ is known, the ion density $n_i$ is deduced from

$$I_{sat} = 0.61 n_i e A_p u_B, \tag{1}$$

where $e$ is the elementary charge, $A_p$ the probe surface area, and $u_B$ the ion Bohm speed. The factor of 0.61 accounts for the presheath-sheath density drop. The probe is mounted at the extremity of an off-center 1.5 m long movable shaft inserted at the downstream end of *Huia* ($z = 120$ cm in Fig. 1). The shaft is covered by a glass sheath to ensure minimum disruption to the predominantly dielectric plasma boundary conditions inside *Huia* [20]. Taking advantage of the axisymmetric geometry of *Huia*, the shaft is simply rotated to produce two-dimensional ($r$-$z$) scans.

A band-pass optical filter centered around 488 nm with a FWHM of 10 nm is used together with a Raspberry Pi camera module as an optical plasma diagnostic. The camera module is based on a color 12 MP Sony IMX477 CMOS sensor. The images were captured in the RAW format using the open-source libcamera library and the rawpy python module in order to by-pass the on-chip post-processing. When filtered, the light gathered by each color channel is extracted and summed together to produce a grayscale image of the scene. The pictures of the plasma in *Huia* are shot radially to produce ($r$-$z$) two-dimensional maps of the glow in broadband visible (VIS) light and for the Ar II relaxation emission at 488 nm.

## Single density peak to double peak mode transition

Two separate studies by Bennet et al. and Filleul et al. performed on *Echidna* and *Huia*, respectively, have both observed a similar behavior when the separation between the antenna and the solenoids center (i.e. $z_B$) is increased beyond some threshold [19, 20]. Interestingly, it was further shown that the working frequency and the type of antenna, whether a double-saddle type or the loop antenna aforementioned, played no role in the mechanisms at work [20]. The key points of this dynamic are summarized here and reproduced from Ref. [20] to pave the way for the next section.

The common configuration found in most magnetized rf plasma devices used for the study of helicon thrusters is with the antenna located in the region of uniform magnetic field (minimum axial gradient) [4, 5]. Figure 3 shows the axial density profile measured in *Huia* in such a configuration when the solenoids are located on top of the antenna ($z_B = 0$ cm, orange curve) for $B_0 = 300$ G. It can be seen that the axial plasma density peaks at $\sim 4 \cdot 10^{17}$ m$^{-3}$ just 2 cm downstream from the loop antenna and then decreases

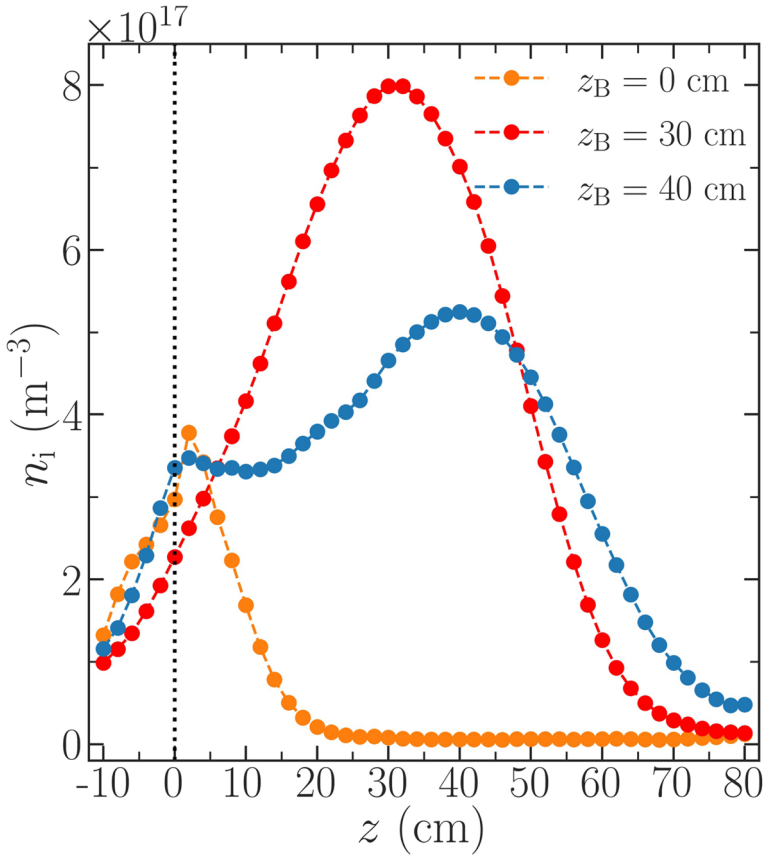


**Fig. 3** Evolution of the axial ion density profiles when the solenoids are located on top of the antenna (orange markers), 30 cm away (red markers) and 40 cm away (blue markers), showing the transition between single to double peak modes. $B_0 = 300$ G for all three cases. The antenna position is marked by the dotted vertical line

closely following the axial decay of $B_0$ (c.f. Fig. 2). This behavior is not surprising as most of the plasma would be created under the antenna and the locally peaking magnetic field would act in reducing the cross-field diffusion and the plasma losses to the walls. As $B_0$ decreases downstream, wall losses would increase and the plasma density decrease in the absence of local plasma creation, as observed in Fig. 3.

When $z_B$ is increased to 30 cm, the axial density profile follows the solenoids and the peak density value is two times higher than when $z_B = 0$ cm. This change in the peak location as well as in the maximum density increase takes place monotonously when $z_B$ is progressively increased [19, 20]. For $z_B > 30$ cm, it is observed that the peak density then decreases and at $z_B = 40$ cm, a second maximum in density appears under the antenna (blue curve in Fig. 3). For larger $z_B$, this double peak mode is observed to persist for $z_B$ up to 60 cm [19, 20].

It should be noted that the ion densities reported in Fig. 3 have been calculated with Eq. 1, using the ion saturation currents measured with the planar langmuir probe and an axially constant electron temperature of $T_e \simeq 4.5$ eV, measured with an rf compensated Langmuir probe for different $z_B$.

Figure 4 shows the 2D ($r$-$z$) maps of the ion saturation. The measurements were carried in the top half of the ($r$-$z$) plane and mirrored for clarity. Figure 4(a) is for the

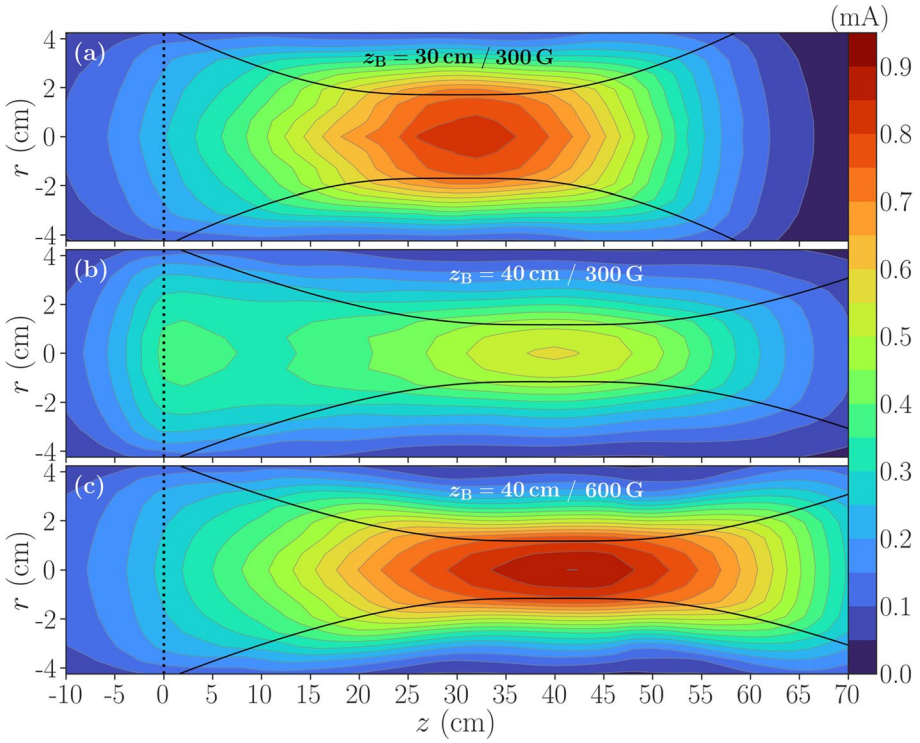


**Fig. 4** 2D mappings of the ion saturation current measured with the planar Langmuir probe when the solenoids are 30 cm away from the antenna and with $B_0 = 300$ G (**a**), when $z_B = 40$ cm and $B_0 = 300$ G (**b**), and $z_B = 40$ cm and $B_0 = 600$ G (**c**). The solid black lines represent the field lines which intersect the glass tube under the antenna at $r = \pm 4.5$ cm and $z = 0$ cm

same conditions as the red curve of Fig. 3, while Fig. 4(b) is for the blue curve. Figure 4(c) is also for $z_B = 40$ cm but at twice the magnetic field intensity $B_0 = 600$ G. It can be observed that the single and double peak features are not restricted to the centreline ($r = 0$ cm), as shown in Fig. 3, but exist on axial profiles for which $|r| \lesssim 1$ cm. More interestingly is the fact that doubling $B_0$ has returned the plasma to the single density peak mode at $z_B = 40$ cm.

The fact that $I_{sat}$ has increased under the solenoids in the $z_B = 40$ cm / $B_0 = 600$ G case compared to $z_B = 30$ cm / $B_0 = 300$ G can be attributed to the radial reduction in the magnetized electron column from the antenna to $z_B$, as the electrons are fully magnetized in the entirety of the probed plasma volume. The electron Larmor radius is indeed still of the order of 1 mm at a distance of 30 cm away from the solenoids and when $B_0 = 300$ G. However something is happening in the $z_B = 40$ cm / $B_0 = 300$ G which is preventing the high density mode to take place.

Combining the radial $I_{sat}$ profiles in Fig. 4 with radial electron temperature profiles acquired with an rf compensated probe (not reported here), one can calculate the average rf skin depth under the antenna to be around 1.2 cm ($\delta_{rf} = c/\omega_{pe}$, with $\omega_{pe}$ the electron plasma frequency). This implies that most of the rf power is deposited in the first 2 cm under the antenna.

### Floating potential and anisotropic wall charging

The observation that a similar mode switching is taking place when the magnetic flux density is increased (c.f. Fig. 4) or when the solenoids are moved away from the antenna (c.f. Fig. 3), whilst the rest of the operating parameters are constant, alludes to the key role played by the plasma magnetization under the antenna. Moreover, it was observed that the mode transition is occuring at the same $z_B$ and $B_0$ regardless of changes in rf power (fromm 200 W to 500 W) or in argon pressure (from 0.5 mTorr to 5 mTorr) [19].

For ions at room temperature and $B_0 = 300$ G, the ion Larmor radius $r_{Li}$ stays smaller than the glass tube internal radius of 4.5 cm up to 32.5 cm away from the solenoids. This distance increases to 41.5 cm when $B_0 = 600$ G. Beyond these points, $r_{Li}$ increases rapidly. Said otherwise, for the cases $z_B = 30$ cm / $B_0 = 300$ G and $z_B = 40$ cm / $B_0 = 600$ G, the ions are fully and partially magnetized between the solenoids ($r_{Li} \simeq 0.5$ cm) and the antenna ($r_{Li} \simeq 3.7$ cm), respectively. For $z_B = 40$ cm / $B_0 = 300$ G however, $r_{Li} \simeq 8$ cm under the antenna and the local ion flux to the wall would be increased in this case. This was previously remarked in Refs. [19, 20] but not supported by measurements of the local charging of the wall.

Figure 5 shows the 2D ($r$-$z$) maps of the plasma floating potential $V_f$ measured with the Langmuir probe for the same conditions as in Fig. 4. It can be seen that the floating potentials behave similarly to $I_{sat}$, i.e. $z_B = 30$ cm / $B_0 = 300$ G and $z_B = 40$ cm /

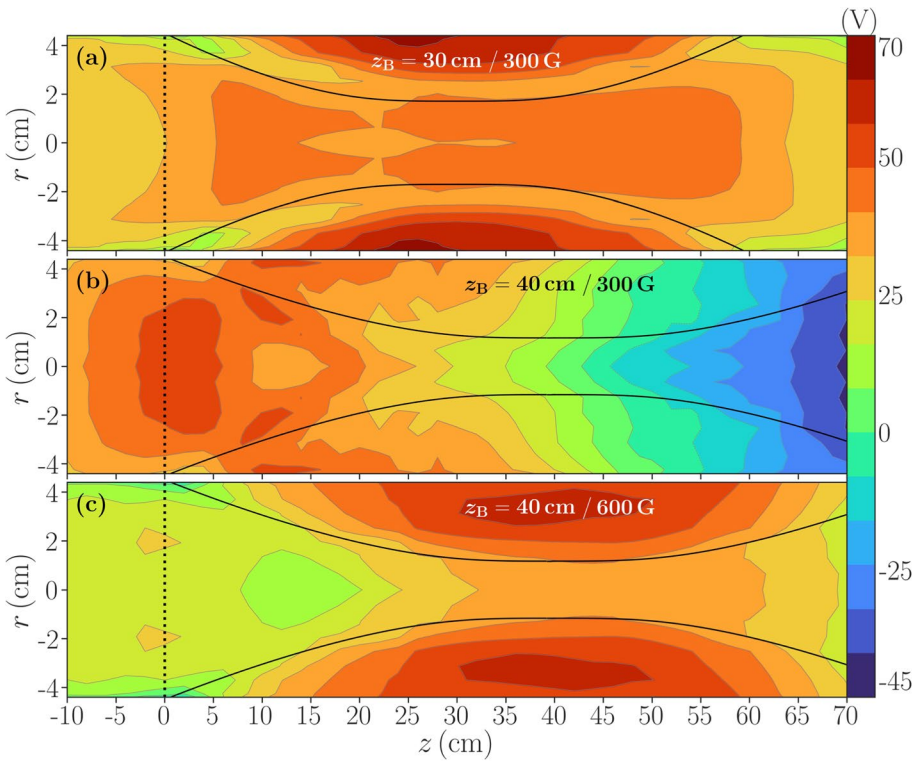


**Fig. 5** 2D mappings of the floating potential $V_f$ measured with the planar Langmuir probe when the solenoids are 30 cm away from the antenna and with $B_0 = 300$ G (**a**), when $z_B = 40$ cm and $B_0 = 300$ G (**b**), and $z_B = 40$ cm and $B_0 = 600$ G (**c**)

$B_0 = 600$ G have very similar $V_f$ features and magnitudes whereas the mapping of $V_f$ for $z_B = 40$ cm / $B_0 = 300$ G portrays a different plasma dynamic.

Noticeably, $V_f$ is relatively constant and uniform in the dense plasma column under the solenoids when the ions are magnetized under the antenna in Fig. 5(a) and (c). Also similar are the islands of maximum $V_f$ above and below, i.e. radially outward from the dense plasma location, which indicates that the glass tube is significantly positively charged under the solenoids. Finally, another interesting feature in these two mappings is the fact that $V_f$ takes its lowest values right under the antenna. The axial scans of $V_f$ taken closest to the glass tube edge at the coordinate $r = 4.3$ cm for the cases $z_B = 30$ cm / $B_0 = 300$ G and $z_B = 40$ cm / $B_0 = 600$ G are plotted in Fig. 6 for better visualization of the anisotropic charging of the glass tube. $V_f$ has clear global minima that match well with the location of the loop antenna at $z = 0$ cm. It should be pointed out that rf sheath dynamics induced by the presence of the antenna could also play a role in the presence and in the magnitude of these local drops in the glass charging [21]. In both cases, the glass tube has a differential charging of around 60 V between the antenna and $z_B$. One last feature worth noting in Fig. 5(a) are the valleys of lower floating potential which follow the last field lines to cross the antenna region. Such a characteristic dip in $V_f$ has been previously associated with the presence of energetic magnetized electrons, presumably excited in the rf skin layer under the antenna and travelling all the way to $z = -60$ cm to potentially contribute to remote ionization [23].

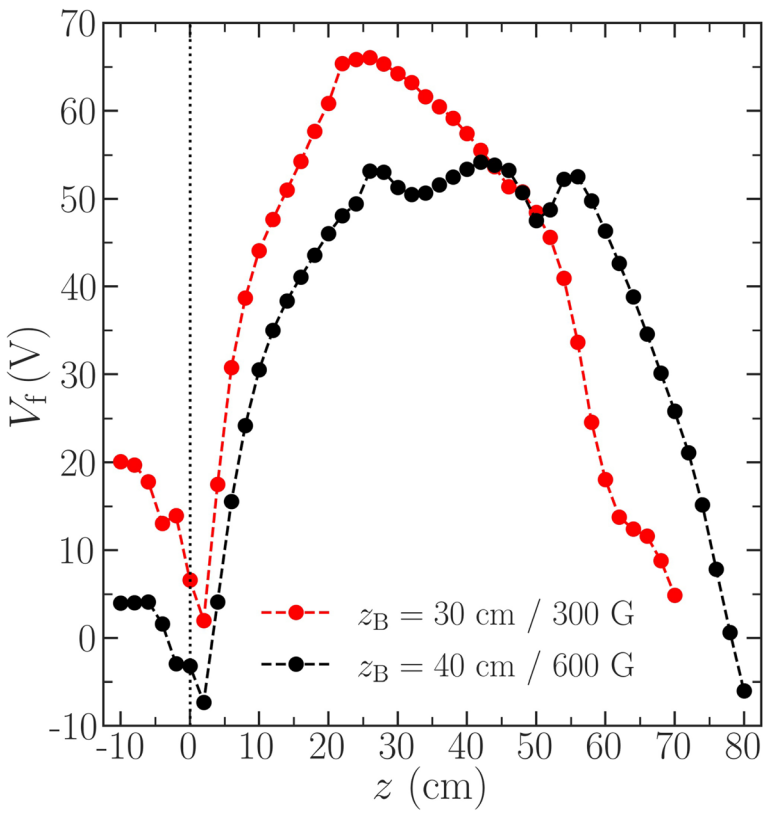


**Fig. 6** Floating potential profiles measured along the glass tube inner surface, at $r \simeq 4.3$ cm for the conditions of Fig. 5(a) and (c) 2DVf

When the ions are not magnetized under the antenna, i.e. for the case $z_B = 40$ cm / $B_0 = 300$ G in Fig. 5(b), while there is still a visible local minimum of $V_f$ under the antenna, the global characteristics of $V_f$ are very different. $V_f$ peaks axially under the antenna and progressively decreases along $z$ to reach $\sim -45$ V downstream of the magnetic nozzle throat. The radial profiles are also more homogeneous with nearly radial $V_f$ isolines in the right-hand side of the MN, contrasting with isolines following the magnetic field lines when the ions are magnetized. Since the floating potential is defined as the potential necessary to equalize the local fluxes of ions and electrons, the region of maximum $V_f$ under the antenna when $z_B = 40$ cm / $B_0 = 300$ G can be interpreted as a region of larger ion flux. This is consistent with the local maximum in ion saturation current under the antenna in Fig. 4(b). The picture emerges where local ions with Larmor radii of the order of 8 cm collide with the glass tube surface before even completing 1/4 of their gyration. The ions will be unable to travel downstream along the field lines and will locally contribute to a more positively charged glass tube. Fewer of the warm and energetic electrons excited some skin depths under the antenna will be able to travel downstream, as a result of being electrostatically trapped under the antenna, inducing a local density peak under the antenna. This reduced transport could at least partly explain why the amplitude of the density peak under the solenoids decreased between $z_B = 40$ cm and $z_B = 30$ cm in Fig. 3.

To complete the picture on the role of the local ion magnetization in the generation of high density plasmas in *Huia*, a Langmuir probe was placed at $r = 4.3$ cm and $z = 0$ cm, i.e. against the glass tube under the antenna, and $B_0$ was progressively increased. The recorded $V_f$ vs $B_0$ characteristics are reported in Fig. 7 for four different values of $z_B$, alongside with the calculated values of $r_{Li}$ under the antenna. The similar shapes and magnitudes of the $V_f$ curves for the four different $z_B$ is striking, suggesting that the local plasma equilibrium conditions are the same in each case but occur for higher $B_0$ as the solenoids are progressively moved away from the antenna. For each $z_B$, the floating potential under the antenna shows a sharper decrease for $B_0$ values which result in $r_{Li} = 4.5$ cm. This observation brings yet another clue of the importance of local ion-source wall dynamics for the global plasma equilibrium. This also suggests that assuming ions at room temperature is a reasonable approximation, at least under the antenna.

A closer look at the different regions of the characteristics in Fig. 7 reveals some insights of the local flux balance as $B_0$ increases. It is worth noting that for all the conditions presented in Fig. 7, the electrons stay magnetized with $r_{Le} \leq 4.5$ mm. $r_{Le}$ is calculated considering $T_e \sim 10$ eV, which was measured under the antenna against the glass tube with an rf compensated probe. In other words, the magnetization effect on the electrons' flux to the wall can be taken as constant in what follows. Changes in $V_f$ are expected to be driven mostly by the level of ion magnetization and electrostatic effects.

When the ions are unmagnetized under the antenna (i.e, $r_{Li} \geq 4.5$ cm), the local $V_f$ asymptotically increases to values around $+50$ V when $B_0$ decreases, which would result in a larger fraction of trapped high-energy electrons and a plasma generation more localized to the antenna region. The trend in $V_f$ with $B_0$ is similar to the trend of $r_{Li}$. Below the $r_{Li} = 4.5$ cm threshold, an increasing fraction of ions are magnetized under the antenna, and fewer will collide with the glass tube during their gyration, making $V_f$ more negative.

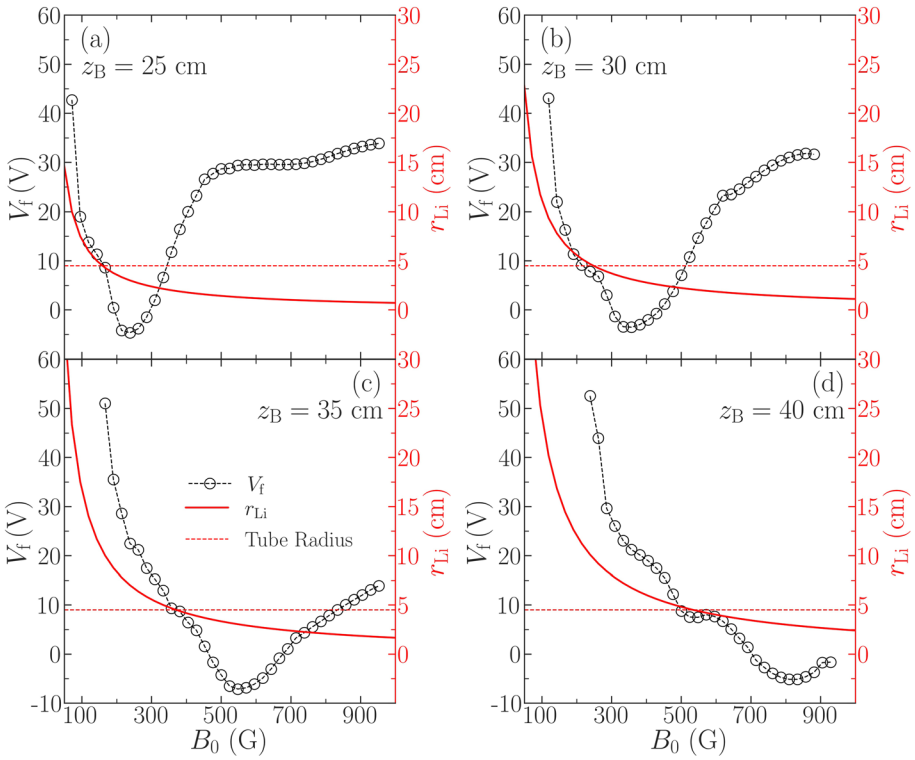


**Fig. 7** $V_f$ (circle symbols, left axis) measured at $z = 0$ cm, i.e. under the antenna by placing the LP right against the glass tube wall as a proxy for the local wall charging when the applied magnetic field is increased. The measurements are repeated for increasing value of $z_B$, from 25 cm (**a**) to 40 cm (**d**), in 5 cm steps. The ion Larmor radius $r_{Li}$ under the antenna (solid line, right axis) is also shown. The horizontal dashed line represents the glass tube inner radius

The minima in $V_f$ in Fig. 7 correspond to an ion gyroradius between approximately 2 and 3 cm. Beyond that point, the floating potential is seen to increase again. The following qualitative picture is proposed as a possible explanation as to why $V_f$ increases again for values of $B_0$ that make $r_{Li} < 2$ cm under the antenna. When $r_{Li} \simeq 2$ cm, ions in the center of the column under the antenna have Larmor orbits grazing the glass tube and will only collide with the glass tube when moving upstream or downstream from this location. This is promoted by the relatively short ion-neutral collision mean free paths ($\sim 3$ cm at 1 mTorr) which would increase the cross-field diffusion. For larger $B_0$, most ions are closely tied to the magnetic field lines as $r_{Li} \sim 1.5$ cm, the minimum value of $r_{Li}$ in the conditions of interest. This could promote the increase in ion flux from ions existing along the streamlines that intersect the glass tube under the antenna. The local ion flux to the glass tube increases again and it is seen to plateau as $r_{Li}$ gets to its minimum value. The plateauing is specially visible in Fig. 7(a). Qualitatively, this is owing to the inhibition of the ion cross-field diffusion. When the field strength is increased to $B_0 = 600$ G for $z_B = 30$ cm, the profile of $V_f$ along the glass tube, not presented in this study, shows that there is no further global minima of $V_f$ under the antenna.

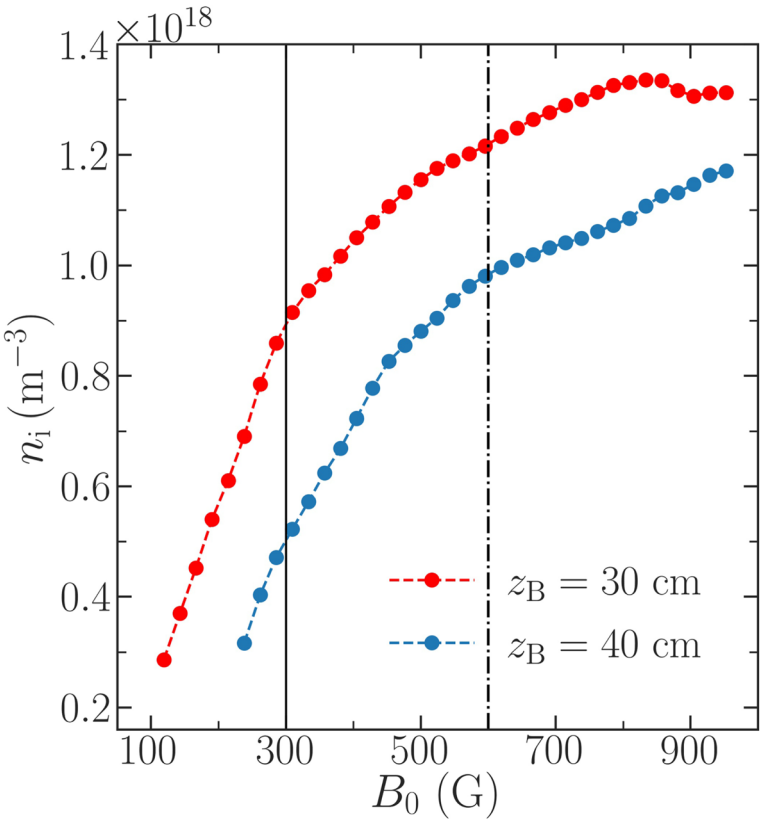


**Fig. 8** Ion density under the solenoids on axis for increasing magnetic density flux, when $z_B = 30$ cm and $z_B = 40$ cm. The vertical continuous and dash-dotted line marks the antenna ion magnetization thresholds for $z_B = 30$ cm and $z_B = 40$ cm, respectively

## High density genereation

Figure 8 shows the ion density on axis under the solenoids, measured with the planar Langmuir probe as $B_0$ is increased, for $z_B = 30$ cm and $z_B = 40$ cm. This figure shows the effectiveness of the plasma generation in the single peak mode. The increase in $n_i$ is the steepest when ions are progressively getting magnetized under the antenna. One continuous and one dash-dotted vertical lines mark the thresholds of ion magnetization under the antenna, as reported in Fig. 7, for $z_B = 30$ cm and $z_B = 40$ cm, respectively. Beyond these thresholds, the rates of increase of $n_i$ with $B_0$ are lower. For $z_B = 30$ cm, $n_i$ eventually reaches a saturation point at $1.3 \cdot 10^{18}$ m$^{-3}$ around 800 G, probably because the plasma cross-field diffusion cannot be further reduced.

Figure 9 shows the light emission of plasma as $B_0$ is increased and with the solenoids placed 30 cm away from the antenna. The two vertical bands in each image are where the plasma emission is blocked by the solenoids. The scene axially spans slightly over 60 cm. In order to give a faithful color representation, the top row in Fig. 9 was produced with the camera with the stock wide bandwidth UV-NIR filter in place. The bottom row images were produced by removing the UV-NIR filter and by placing the 488 nm filter in front of the objective lens.

It is visible in both rows that the plasma stays mostly confined to the antenna region when $B_0 = 75$ G. At higher magnetic fields, the plasma luminosity increases

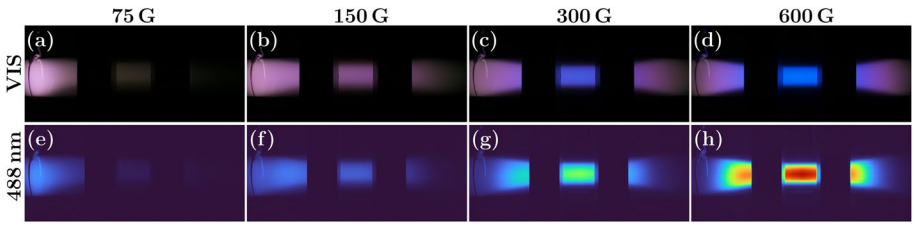


**Fig. 9** The top row **a**-**d** shows the evolution of the plasma discharge along the glass tube in broadband visible light as $B_0$ is increased at a fixed power of 200 W, an argon pressure of 1 Torr and $z_B = 30$ cm. The loop antenna is visible as a thin black line at the extreme left of each picture. The bottom row **e**-**h** shows the same scene but captured again through the 488 nm filter. The camera's shutter speed was set at 1/125 s while the analog and digital gain of the sensor were fixed to unity. The white balance was kept constant for the VIS light photographs, and is irrelevant for the filtered ones

downstream and from 300 G onward the characteristic blue light of the Ar II emissions starts to dominate inside the collimated column under the solenoids (c.f. Fig. 9(c) and (d)). At 600 G, a blue core is formed, which is evident with the strong 488 nm light intensity in Fig. 9(h).

Excitation of an argon ion to a state which then decays by emitting a 488 nm photon can either happen from a direct electron-neutral collision or through a electron-ion collision [24]. However, the latter is 15 to 30 times more efficient than the former [25]. Therefore, most of the 488 nm light seen can be attributed to electron-ion collisions. Moreover, this process has a threshold in electron energy of 17 to 20 eV [24, 26]. Hence, the Ar II light in Fig. 9 is likely a sign of the presence of electrons in the inelastic range far downstream from the antenna, especially since the excited ion state which can emit the 488 nm photon has a lifespan of a few nanoseconds, i.e. far shorter than the travel time of thermal ions from the antenna to the solenoids [27]. Ions created under the antenna are also unlikely to efficiently travel downstream as the ion-neutral collision mean-free paths are around 3 cm at the present working pressure. The sign of a significant fraction of electrons in the inelastic range beyond $z_B$ is suggestive of the non-local plasma ionization in *Huia* taking place due to the transport of high-energy electrons from the antenna.

The continuous increase in the Ar II light intensity under the solenoids with $B_0$ matches the trend of the measured ion density in Fig. 8. The onset of a wave-heated mode is often associated with the observation of a step increase in plasma density with $B_0$ [28]. Since no such step increase was observed here, nor wave modes identified in Echnida [19], the data from Figs. 9 and 8 support the hypothesis that the remote ionization far from the antenna could be due to the downstream transport of electrons energized under the antenna. Such energetic electrons have been measured with the rf compensated probe and will be the focus of a future work.

## Conclusion

Volumetric and localized in-situ measurements, as well as non-disruptive optical measurements, are presented to explore plasma modes in a long converging-diverging magnetized rf column. The experimental conditions can be taken as a proxy of the conditions

existing in the source tube of a magnetic nozzle rf thruster before the plasma expands into space.

Two modes of operation are observed. The first one has a single axial high density peak coinciding with the location of maximum magnetic field. The second mode sees the density being double-peaked on axis, with one peak under the antenna and a second under the solenoids. The transition between the two modes takes place either when the solenoids are moved farther away from the antenna at a constant magnetic field, or when the magnetic field flux density is decreased for a given solenoid position. A strong correlation is observed between the level of ion magnetization under the rf antenna and the plasma being in one mode or the other. This is further supported by measurements of the plasma floating potential under the antenna, $\sim 1.5$ mm away from the glass tube, showing changes in the local glass tube charging that match well with the local ion gyroradius becoming smaller than the glass tube radius. When ions are unmagnetized under the antenna, while electrons are always magnetized, the local flux balance causes the glass tube to be locally strongly positively charged, resulting in an electrostatic trapping of high-energy electrons that would have otherwise traveled far downstream. This causes the plasma to be in a double-peaked mode. In the single peak mode, densities up to $10^{18}$ $m^{-3}$ and strong Ar II emission are observed at a modest rf power of 200 W and a magnetic field of at least 400 G. This is seen as a sign of efficient plasma generation in a large volume far from the rf antenna. The observation of intense Ar II emission at 488 nm is also an evidence that electrons in the inelastic range are efficiently travelling far away from the antenna or are remotely excited.

These results highlight the importance of considering the levels of ion magnetization in the source tube of a magnetic nozzle rf thruster. In particular, obtaining high plasma densities at moderate rf powers would be beneficial for achieving a high propellant utilization fraction and thruster efficiency.

**Acknowledgements**
None

**Authors' contributions**
FF developed the apparatus, acquired the data, conceptualized and wrote the manuscript. AC helped in the data acquisition and the construction of the apparatus. RB and CC provided guidance in experimental RF plasmas and diagnostics and feedback on the manuscript. NR and JC are doctoral supervisors of FF and AC and gave feedback on the manuscript. All authors read and approved the final manuscript.

**Funding**
This work was partially funded by the New Zealand Space Agency under MBIE contract #00008060.

**Availability of data and materials**
The data that support the findings of this study are available from the corresponding author upon reasonable request.

## Declarations

**Competing interests**
The authors declare that they have no competing interests.

Received: 3 August 2022 Accepted: 12 October 2022
Published online: 04 November 2022

**References**

1. Charles C (2009) Plasmas for spacecraft propulsion. J Phys D Applied Phys 42(16):163001. https://doi.org/10.1088/0022-3727/42/16/163001
2. Lemmer K (2017) Propulsion for CubeSats. Acta Astronaut 134:231–243. https://doi.org/10.1016/j.actaastro.2017.01.048

3. Takahashi K (2021) Magnetic nozzle radiofrequency plasma thruster approaching twenty percent thruster efficiency. Sci Rep 11(1):1–12. https://doi.org/10.1038/s41598-021-82471-2
4. Charles C, Boswell R (2003) Current-free double-layer formation in a high-density helicon discharge. Appl Phys Lett 82(9):1356–1358. https://doi.org/10.1063/1.1557319
5. Takahashi K (2019) Helicon-type radiofrequency plasma thrusters and magnetic plasma nozzles. Rev Mod Plasma Phys 3(1):1–61. https://doi.org/10.1007/s41614-019-0024-2
6. Charles C (2010) High density conics in a magnetically expanding helicon plasma. Appl Phys Lett 96(5):051502. https://doi.org/10.1063/1.3309668
7. Bennet A, Charles C, Boswell R (2018) Selective radial release of hot, magnetised electrons downstream of a low-pressure expanding plasma. J Phys D Appl Phys 51(37):375204. https://doi.org/10.1088/1361-6463/aad74f
8. Caldarelli A, Filleul F, Charles C, Boswell R, Rattenbury N, Cater J (2022) Radial characterization of an ion beam in a deflected magnetic nozzle. J Electr Propuls 1(10). https://doi.org/10.1007/s44205-022-00012-z
9. Takahashi K, Sugawara T, Ando A (2020) Spatial measurement of axial and radial momentum fluxes of a plasma expanding in a magnetic nozzle. New J Phys 22(7):073034. https://doi.org/10.1088/1367-2630/ab98d5
10. Ahedo E, Merino M (2010) Two-dimensional supersonic plasma acceleration in a magnetic nozzle. Phys Plasmas 17(7):073501. https://doi.org/10.1063/1.3442736
11. Takahashi K, Akahoshi H, Charles C, Boswell RW, Ando A (2017) High temperature electrons exhausted from rf plasma sources along a magnetic nozzle. Phys Plasmas 24(8):084503. https://doi.org/10.1063/1.4990110
12. Takahashi K, Sugawara T, Ando A (2020) Spatially-and vector-resolved momentum flux lost to a wall in a magnetic nozzle rf plasma thruster. Sci Rep 10(1):1–11. https://doi.org/10.1038/s41598-020-58022-6
13. Emoto K, Takahashi K, Takao Y (2021) Vector resolved energy fluxes and collisional energy losses in magnetic nozzle radiofrequency plasma thrusters. Front Phys 676. https://doi.org/10.3389/fphy.2021.779204
14. Charles C, Boswell R (2007) The magnetic-field-induced transition from an expanding plasma to a double layer containing expanding plasma. Appl Phys Lett 91(20):201505. https://doi.org/10.1063/1.2814877
15. Takahashi K, Charles C, Boswell RW, Fujiwara T (2010) Double-layer ion acceleration triggered by ion magnetization in expanding radiofrequency plasma sources. Appl Phys Lett 97(14):141503. https://doi.org/10.1063/1.3499653
16. Takahashi K, Charles C, Boswell RW (2013) Approaching the theoretical limit of diamagnetic-induced momentum in a rapidly diverging magnetic nozzle. Phys Rev Lett 110(19):195003. https://doi.org/10.1103/PhysRevLett.110.195003
17. Little JM, Choueiri EY (2014) Critical condition for plasma confinement in the source of a magnetic nozzle flow. IEEE Trans Plasma Sci 43(1):277–286. https://doi.org/10.1109/TPS.2014.2322522
18. Yadav S, Ghosh S, Bose S, Barada KK, Pal R, Chattopadhyay PK (2018) Role of ion magnetization in formation of radial density profile in magnetically expanding plasma produced by helicon antenna. Phys Plasmas 25(4):043518
19. Bennet A, Charles C, Boswell R (2019) Non-local plasma generation in a magnetic nozzle. Phys Plasmas 26(7):072107. https://doi.org/10.1063/1.5098484
20. Filleul F, Caldarelli A, Charles C, Boswell R, Rattenbury N, Cater J (2021) Characterization of a new variable magnetic field linear plasma device. Phys Plasmas 28(12):123514. https://doi.org/10.1063/5.0070924
21. Butler H, Kino G (1963) Plasma sheath formation by radio-frequency fields. Phys Fluids 6(9):1346–1355. https://doi.org/10.1063/1.1706905
22. Merlino RL (2007) Understanding Langmuir probe current-voltage characteristics. Am J Phys 75(12):1078–1085. https://doi.org/10.1119/1.2772282
23. Igarashi Y, Takahashi K, Fujiwara T (2011) Energetic electrons moving along peripheral magnetic field lines in magnetically expanding plasmas. IEEE Trans Plasma Sci 39(11):2442–2443. https://doi.org/10.1109/TPS.2011.2143432
24. Blackwell DD, Chen FF (1997) Two-dimensional imaging of a helicon discharge. Plasma Sources Sci Technol 6(4):569. https://doi.org/10.1088/0963-0252/6/4/015
25. Imre A, Dashchenko A, Zapesochnyi I, Kel'Man V (1972) Cross Sections for the Excitation of Ar II Laser Lines in Electronion Collisions. Sov J Exp Theor Phys Lett 15:503
26. Vincent S, Dolique V, Plihon N (2022) High-speed imaging of magnetized plasmas: When electron temperature matters. Physics of Plasmas 29(3):032104. https://doi.org/10.1063/5.0083130
27. Luyken B (1972) Transition probabilities and radiative lifetimes for Ar II. Physica 60(2):432–458. https://doi.org/10.1016/0031-8914(72)90114-0
28. Degeling A, Jung C, Boswell R, Ellingboe A (1996) Plasma production from helicon waves. Phys Plasmas 3(7):2788–2796. https://doi.org/10.1063/1.871712


## Publisher's Note

JOURNAL OF SPACECRAFT AND ROCKETS
Vol. 59, No. 6, November–December 2022

# Low-Thrust Trajectory Design from Lunar Rideshare to Venus Capture

Darcey R. Graham*
*The University of Auckland, Auckland 1010, New Zealand*
Jacob A. Englander†
*Johns Hopkins Applied Physics Laboratory, Laurel, Maryland 20723*
and
Nicholas J. Rattenbury‡ and John E. Cater§
*The University of Auckland, Auckland 1010, New Zealand*

https://doi.org/10.2514/1.A35282

**Small spacecraft are likely to be launched as part of a rideshare mission rather than on a dedicated launch. These spacecraft typically use low-thrust propulsion systems as they have lower fuel mass requirements. However, without a dedicated launch, the lower thrust can make it difficult to reach interplanetary targets. Further mission design difficulties arise as the optimizers used to search for such trajectories often require a good initial guess, which can be difficult to find. This work patches together a perturbed Sims–Flanagan transcription in three different regimes, each with a different central body, to perform a preliminary search for trajectories from a lunar rideshare to a weak capture around Venus with little input required from the mission designer. Example trajectories of such a mission are presented. The ability of this mission architecture to arrive as close to Venus's upper atmosphere as possible is explored.**



## Nomenclature

| | | |
|---|---|---|
| $\boldsymbol{c}$ | = | constraint function |
| $D$ | = | thruster duty cycle |
| $F$ | = | Lagrange multiplier |
| $f_{\text{objective}}$ | = | objective function |
| $G$ | = | another Lagrange multiplier |
| $g_0$ | = | acceleration due to gravity at Earth's surface, km/s$^2$ |
| $h_{\text{safe}}$ | = | safe height above a massive body, km |
| $I_{\text{sp}}$ | = | specific impulse, s |
| $m$ | = | spacecraft total mass, kg |
| $\dot{m}$ | = | fuel mass flow rate, kg/s |
| $N$ | = | number of segments in a Sims–Flanagan trajectory phase |
| $N_{\text{active}}$ | = | number of active thrusters |
| $N_{\text{p}}$ | = | number of Sims–Flanagan phases in a full trajectory |
| $\boldsymbol{r}$ | = | spacecraft position relative to central body, km in Cartesian coordinates |
| $r_{\text{body}}$ | = | radius of a massive body, km |
| $r_{\text{periapse}}$ | = | periapse radius of an orbit, km |
| $r_{\text{SOI}}$ | = | radius of the sphere of influence of a massive body, km |
| $T$ | = | thrust, kN |
| $U$ | = | universal variable in Keplerian propagation |
| $\boldsymbol{u}$ | = | thrust control vector, unitless in Cartesian coordinates |
| $\boldsymbol{v}$ | = | spacecraft velocity relative to central body, km/s in Cartesian coordinates |
| $v_\infty$ | = | excess velocity relative to a massive body, km/s |
| $\boldsymbol{X}$ | = | spacecraft state vector, contains position, velocity, and mass |
| $\alpha$ | = | inverse of semimajor axis |
| $\Delta t$ | = | time of flight of a trajectory phase, s |
| $\Delta v$ | = | change in velocity due to an impulse, km/s |
| $\delta$ | = | turn angle of gravity assist, rad |
| $\mu$ | = | standard gravitational parameter of a massive body, km$^3$/s$^2$ |
| $\chi$ | = | universal anomaly |

*Subscripts*

| | | |
|---|---|---|
| $B$ | = | final value in backward-shooting arc |
| cp | = | central body to perturbing body |
| $F$ | = | final value in forward-shooting arc |
| $k$ | = | index of trajectory segment |
| $p$ | = | perturbing body |

*Superscripts*

| | | |
|---|---|---|
| $+$ | = | value immediately following an impulse |
| $-$ | = | value immediately before an impulse |

Received 12 October 2021; revision received 1 June 2022; accepted for publication 3 August 2022; published online 19 September 2022. 

*Ph.D. Student, Department of Physics, Private Bag 92019.
†Mission Design Engineer, Space Exploration Sector, 11101 Johns Hopkins Road.
‡Department of Physics, Private Bag 92019.
§Department of Engineering Science, Private Bag 92019.

## I. Introduction

PRELIMINARY trajectory design for spacecraft using low-thrust propulsion systems is a challenging optimization problem. In high-thrust systems, maneuvers can be approximated as occurring instantaneously. In contrast, low-thrust events last days or weeks, as lower thrust takes more time to significantly change the spacecraft's velocity. An instantaneous approximation is no longer appropriate. Thrust must instead be modeled as continuous, so acceleration due to thrust must be included in the equations of motion, increasing the complexity of the problem. When carrying out a global search for feasible trajectories, computation time is important as many different trajectories must be computed and examined to find a feasible solution. Simplified equations of motion are preferred to reduce the computation time.

This work patches together perturbed Sims–Flanagan trajectories from three different regimes, each regime a different two-body problem with a different central body. A preliminary search is conducted for low-thrust trajectories to Venus. The model includes escape from the Earth–moon system and capture at Venus. This work presents, for the first time, the solution of a perturbed Sims–Flanagan-based trajectory that passes through regimes with three different central bodies solved in one problem, as well as the application to a low-thrust Venus mission

from lunar rideshare. The aims of this work are to solve different parts of a trajectory in one problem, to conduct a preliminary search for Venus trajectories requiring little input from a mission designer, and to demonstrate what can be accomplished by low-thrust systems. In this case a relatively small 180 kg spacecraft using a Hall thruster capable of 39 mN of thrust, with a specific impulse of 1500 s, is used. Small spacecraft are unlikely to be granted dedicated launches onto interplanetary trajectories. However, interplanetary space is not completely inaccessible to smaller spacecraft with low thrust, as gravity assists can provide the changes in energy needed to reach ambitious targets [1]. The mission presented here starts with injection from a lunar ride share, escapes the Earth–moon system using two lunar gravity assists (LGAs), and arrives into a weak capture at Venus.

Venus was chosen as the target mission due to the increasing scientific interest in Venus missions. Studies of the Venusian atmosphere could reveal much to atmospheric science as well as inform our understanding of the evolution of our own planet. Venus was potentially Earth-like until a few hundred million years ago; therefore by studying its atmosphere we might better understand the future of our own planet, and may also answer questions regarding similar exoplanets [2]. With new Venus missions such as the ISRO's Shukrayaan-1 and NASA's Discovery missions DAVINCI+ and VERITAS [3–5], Venus is growing increasingly relevant as a target.

To find feasible trajectories, the trajectory is posed as an optimization problem. The criteria to decide which solution to the optimization problem is the "best" depend on the mission. Here, it means the solution with the lowest fuel expenditure. Many optimization problems require a good initial guess for the values of the decision variables in order to converge on a locally optimal solution. Guesses are difficult to produce as many variables are physically nonintuitive. As a result, some less apparent trajectory designs may be overlooked. To overcome this difficulty, a global search with a low-fidelity solver can be performed. This search can be robust to the initial guess, and the solutions can be used as an initial guess in turn by a higher-fidelity solver [6].

Careful selection of the optimization method can also aid in solving the problem. Many different types exist, typically classified as indirect or direct techniques. Indirect methods solve for the state and costate vectors [7,8]. Although indirect methods give more accurate solutions than direct methods, they are more sensitive to the initial guess, so are less suited to the problem posed here. Direct methods convert the problem to a nonlinear programming (NLP) problem to be solved by an NLP solver [9–11], as done in this work. By solving the optimization problem as an NLP problem within a monotonic basin hopping (MBH) algorithm [12,13], a large problem space can be explored. This makes the optimizer less sensitive to the initial guess.

There is a drive toward autonomous preliminary searches to make preliminary search easier, for example, for onboard trajectory design [14]. Bounds on decision variables are given by the mission designer for each decision variable. The model generates decision variables from a uniform distribution within bounds set by the mission designer. These bounds can be wide to reduce the workload of the mission designer. For example, a range in flight times could be from a few days to thousands of days, or the start and final points of a trajectory could be bound to be anywhere within a planet's sphere of influence (SOI). The other information supplied by the mission designer is the target planet, any gravity assists, and information on the spacecraft: namely, maximum thrust, specific impulse, thrust duty cycle, and number of thrusters active.

Numerous methods have been used in the past to find interplanetary trajectories. For example, the circular restricted three-body problem (CRTBP) models two massive bodies such as the Earth and moon as well as the spacecraft moving in their vicinity. The dynamics in this approach are more accurately modeled than the two-body problem, as in the two-body problem the effects of additional celestial bodies are approximated as perturbations. As a result, the CRTBP can take advantage of dynamic features such as manifolds [15,16]. However, the increased complexity increases computation time and sensitivity to the initial guess, making CRTBP models less practical for a wide preliminary search. Some have worked around this by computing information about the dynamic structures present to use as part of an initial guess [17], or by using optimization algorithms that search a wide problem space, such as evolutionary algorithms and reinforcement learning [18]. Other methods used to find interplanetary trajectories include shape-based methods [14,19], which assume the shape of the trajectory to save computation effort, but may request too high thrust, and solutions to the Stark model, which divides the trajectory into segments similar to the Sims–Flanagan transcription, but is integrable [20]. Trajectories patching together different regimes have been used before [1], including to Venus, but not using the Sims–Flanagan transcription as used here.

This work uses a variant of the Sims–Flanagan transcription [21,22]. This is a bounded-impulse model, meaning that thrust is approximated as a series of discrete instantaneous impulses. With a large enough number of impulses, the thrust profile becomes approximately continuous. Between impulses the spacecraft motion is modeled as Keplerian. Although high-fidelity models do not make this approximation, it is useful for performing a global search for feasible trajectories that can then be refined by a higher-fidelity optimizer searching in a small local region of the problem space. The perturbed Sims–Flanagan transcription is not new, though applying the $n$-body perturbed model to this mission scenario is. Others have used the Sims–Flanagan transcription to solve interplanetary trajectories before [11]. These cases did not include the escape and arrival phases in the problem, looking instead at the interplanetary sun-centered regime of the trajectory.

This paper is outlined as follows: First, the physical model used to determine the motion of the spacecraft will be described. The modeling of gravity assists will also be described, as will the division of the overall Earth–Venus trajectory into three stages. In the following section, the optimization method will be explained by defining the NLP problem with its constraints and decision variables, then the MBH algorithm will be outlined. Example results for two trajectories will be presented. Finally, an exploration will be made to find any tradeoffs between final mass and the closest distance to Venus's surface, and the model will be verified against existing solutions in literature.

## II. Modeling

### A. Trajectory Model

The trajectories designed here are divided into three stages, each containing one or more trajectory phase patched together. Figure 1 illustrates one phase, which is adapted from the Sims–Flanagan transcription. Each phase starts and ends with a control node, a point where the spacecraft state vector—its position, velocity, and mass—is defined as decision variables (also called control variables). The state vector is then propagated forward in time from the start node, and backward in time from the final node. The two arcs are forced to meet halfway through in time at a match point. The final node of one phase is the start node of the next phase to maintain continuity. Nodes can be celestial bodies, gravity assists, or free points in space. Each phase is split further into segments, with the trajectory propagated forward or backward segment by segment. Continuous thrust can then be approximated as a series of instantaneous impulses spaced closely together in time. One impulse occurs at the center of each segment. Other perturbing forces can likewise be included in these impulses, modeled as an instantaneous change in spacecraft mass and velocity.

Between impulses, the trajectory is propagated forward and backward in time using Kepler's equation [23]. Two-body dynamics are assumed, where the spacecraft is one body of negligible mass, and the massive body it is orbiting (the Earth, sun, or Venus) is the other body, called the central body and positioned at the origin. Figure 1 shows how the spacecraft state vector is propagated. Red arrows indicate thrust and teal arrows indicate perturbing forces. These forces are applied together at the same time at the impulses. Green lines indicate where segments are divided, and the blue arrows indicate Keplerian propagation. In forward shooting, the position and velocity vectors are propagated from the point immediately after one impulse, located at the red and teal arrows, through to the point in time at which the

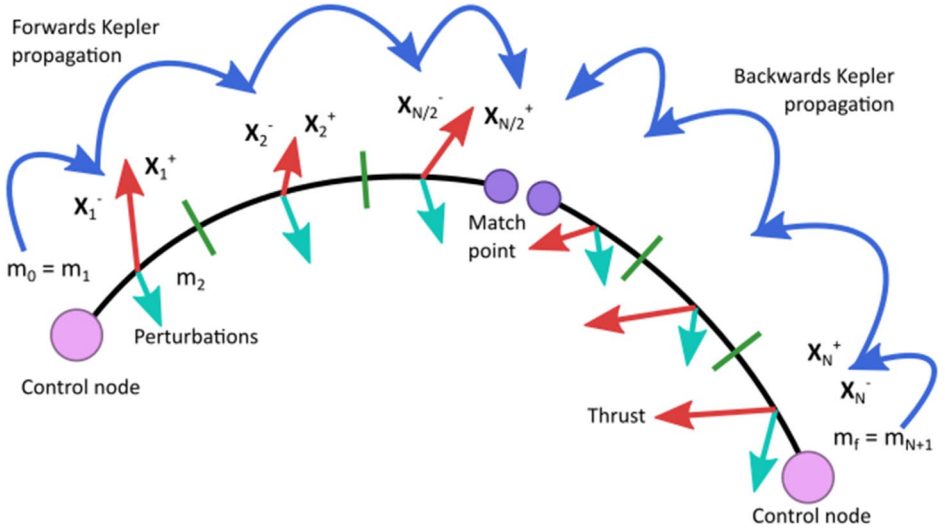


**Fig. 1 A single trajectory phase showing division into $N$ segments with impulses at the segment center. $X_k^{\pm}$ indicates the state vector before (−) and after (+) each impulse, and $m$ is the spacecraft mass.**

following impulse occurs. In backward shooting, this is done in reverse. The position and velocity are propagated backward in time from just before one impulse to just after the previous impulse. Impulses are instantaneous, so for a given impulse there is no change at an impulse, but there is a change in mass and velocity.

To solve Kepler's equation, this work makes use of universal variables [24] coupled with the Laguerre–Conway root-finding method [25]. Spacecraft position and velocity at the next (or previous, for backward shooting) impulse are propagated to by solving for them iteratively based on the current position and velocity. The alternative is to solve for them by explicit integration. Solving iteratively is computationally faster. Universal variables make the solution applicable to trajectories of any conic section, rather than just elliptical orbits. The Laguerre–Conway method was chosen as it converges rapidly to a solution even given a poor initial guess [25].

In this form of Keplerian propagation, the universal anomaly $\chi$ is found iteratively by the Laguerre–Conway root-finding method, then used to find the universal variables. Universal variables must be defined differently depending on whether the orbit is elliptical, parabolic, or hyperbolic. Equations (2–7) are used depending on the type of orbit as determined by the inverse of the semimajor axis:

$$\alpha = \frac{1}{\alpha} = \frac{2}{r_k} - \frac{v_k^2}{\mu} \tag{1}$$

The universal variables for an elliptical orbit, for which $\alpha > 0$, are then

$$U_1 = \chi(1 - yS), \qquad U_2 = \chi^2 C, \qquad U_3 = \chi^3 S,$$
$$U_0 = 1 - \alpha U_2 \tag{2}$$

where

$$y = \alpha\chi^2 \tag{3}$$

$$S = \frac{1}{y^{3/2}}(\sqrt{y} - \sin(\sqrt{y})) \tag{4}$$

$$C = \frac{1}{y}(1 - \cos(\sqrt{y})) \tag{5}$$

For parabolic orbits, where $\alpha = 0$,

$$U_0 = 1, \qquad U_1 = \chi, \qquad U_2 = \frac{U_1\chi}{2}, \qquad U_3 = \frac{U_2\chi}{3} \tag{6}$$

For hyperbolic orbits, where $\alpha < 0$,

$$U_0 = \cosh(\sqrt{-\alpha}\chi), \qquad U_1 = \frac{1}{\sqrt{-\alpha}}\sinh(\sqrt{-\alpha}\chi),$$
$$U_2 = \frac{1}{\alpha}(1 - U_0), \qquad U_3 = \frac{1}{\alpha}(\chi - U_1) \tag{7}$$

Universal variables, found according to the conic section present in the current orbit, are then used to find the Lagrange coefficients and their time derivatives:

$$F = 1 - \frac{U_2}{r_k}$$
$$\dot{F} = 1\frac{\sqrt{\mu}}{r_{k+1}r_k}U_1$$
$$G = \frac{1}{\sqrt{\mu}}(r_k U_1 + \sigma_0 U_2)$$
$$\dot{G} = 1 - \frac{U_2}{r_{k+1}} \tag{8}$$

where

$$\sigma_0 = \frac{\boldsymbol{r}_k \cdot \boldsymbol{v}_k}{\sqrt{\mu}} \tag{9}$$

and the magnitude of the spacecraft position vector is propagated by

$$r_{k+1} = r_k U_0 + \sigma_0 U_1 + U_2 \tag{10}$$

Finally, the position and velocity vectors can be propagated forward to a later point in time using the Lagrange coefficients. This is done to take the state vector from the point just after the impulse in one segment to the point just before the impulse in the next segment. Performing this in reverse results in backward propagation.

For forward propagation,

$$\begin{bmatrix} \boldsymbol{r}_{k+1} \\ \boldsymbol{v}_{k+1} \end{bmatrix} = \begin{bmatrix} F & G \\ \dot{F} & \dot{G} \end{bmatrix} \begin{bmatrix} \boldsymbol{r}_k \\ \boldsymbol{v}_k \end{bmatrix} \tag{11}$$

The impulse at the center of each segment enforces the effect of any perturbations to the system. In this model, perturbing forces are due to thrust and $n$-body gravitational perturbations. Thrusting, the only component of the impulse in this work that affects spacecraft mass is controlled using the thrust control vector $\boldsymbol{u}$. The magnitude of the impulse is equal to the total change that would occur over the time

interval of the segment. This informs the choice to place impulses at the center of each segment. Positioning an impulse at the center of the segment gives the smallest maximum distance in time between the impulse and the edge of the segment, improving the accuracy of approximating the entire effect of perturbations and thrust across the segment at a single point in time. Increasing the number of segments each phase will increase accuracy by increasing the frequency with which the direction of the position and velocity vectors of the perturbing bodies is updated. The mass following an impulse is

$$m_k = \begin{cases} m_{k-1} - \|\boldsymbol{u}_{k-1}\| D \Delta t_k \dot{m}_{\max_k} & \text{forward propagation} \\ m_{k+1} + \|\boldsymbol{u}_k\| D \Delta t_k \dot{m}_{\max_k} & \text{backward propagation} \end{cases} \tag{12}$$

where duty cycle $D$ is the percentage of time during a thrust arc that the thrusters are switched on. Here it was assumed to be unity, though in practice this will not be the case. The maximum mass flow rate $\dot{m}_{\max_k}$ is

$$\dot{m}_{\max_k} = \frac{T_{\max}}{I_{\text{sp}} g_0} \tag{13}$$

The maximum thrust available $T_{\max}$ is another value determined by the thruster used. Its value may depend on the power available from the spacecraft's power source, but for this study it was kept constant for to keep the problem simple at this low-fidelity stage, and because the spacecraft is moving closer to the sun to reach Venus, so solar power would increase to closer to the maximum. Kepler's equation uses a two-body model, but in reality the gravitational forces of other celestial bodies act on the spacecraft. Expending fuel is the only process changing mass at the impulse, but velocity is also affected by $n$-body gravitational perturbations. The effect of thrust events is modeled using the maximum possible change in velocity over the time of the entire segment, modified by the thrust control vector to allow throttling. The maximum change in velocity due to thrust before throttling is

$$\Delta v_{\max_k} = \frac{N_{\text{active}} D T_{\max} \Delta t_k}{m_k} \tag{14}$$

where $N_{\text{active}}$ is the number of active thrusters on the spacecraft. In this work, it was set to unity to simplify the problem, assuming that the small spacecraft has only one thruster firing at a time.

The total change in velocity at a given impulse due to thrust and $n$-body gravity is then

$$\begin{aligned} \boldsymbol{v}_k^+ &= \boldsymbol{v}_k^- + \Delta v_{\max_k} \boldsymbol{u}_k \\ &\quad + \sum_{p=1}^{n} \left[ -\frac{\mu_p \boldsymbol{r}_p}{r_p^3} \Delta t_k + \frac{\mu_p \boldsymbol{r}_{\text{cp}}}{r_{\text{cp}}^3} \Delta t_k \right] \text{ forward shooting} \\ \boldsymbol{v}_k^- &= \boldsymbol{v}_k^+ - \Delta v_{\max_k} \boldsymbol{u}_k \\ &\quad - \sum_{p=1}^{n} \left[ -\frac{\mu_p \boldsymbol{r}_p}{r_p^3} \Delta t_k + \frac{\mu_p \boldsymbol{r}_{\text{cp}}}{r_{\text{cp}}^3} \Delta t_k \right] \text{ backward shooting} \end{aligned} \tag{15}$$

where all vectors are given in Cartesian coordinates with the central body at the origin.

In Eq. (15), the second term is the change in velocity due to thrusting. The third term is the effect of the perturbing body on the spacecraft. The fourth term accounts for the gravitational forces of the perturbing and central bodies acting on each other.

Ephemeris data for the Earth, moon, Venus, and sun were provided by NASA's SPICE toolkit [26,27]. Calling SPICE with each iteration of the optimizer increases computation time by several hours. Instead, SPICE data are initially queried over a wide range of dates outside the optimizer. These values are passed to the optimizer, then interpolated over the time of flight to allow a flexible epoch and flight time without compromising computation time. This is done by supplying the optimizer with ephemeris data over dates from the earliest permitted launch date to the latest permitted launch date plus the total maximum time of flight, and the epochs at which each data point is taken. Within the optimizer, MATLAB's *spline* function is then used to interpolate ephemeris data to find the positions and velocities of all perturbing bodies at the epochs of each Sims–Flanagan segment.

### B. Gravity Assists

Two LGAs occur in the example trajectories presented here. The number of gravity assists was not allowed to change within the model, though it is possible to use this model for different mission architectures, as will be demonstrated later in this work. A single LGA is typically unable to provide the change in spacecraft velocity needed for it to leave the Earth's SOI. With two, a greater change can be made, permitting the spacecraft to escape the Earth–moon system. Constraints are applied to the NLP problem to ensure that the change in velocity is physically realizable, as will be described later in Eqs. (19–21). They ensure that conservation of momentum is maintained and that the spacecraft does not crash into the surface of the moon.

Gravity assists are modeled using a zero SOI patched-conic approximation. This means that the gravity assist is modeled as instantaneous. It also does not switch to a moon-centered model, occurring entirely within the Earth-centered system. The moon's position is taken at the epoch at which the gravity assist occurs. This location, in Cartesian coordinates, is the position of the spacecraft at the control node of a Sims–Flanagan phase. Upon reaching this point in space, the gravity assist is applied as an instantaneous change in spacecraft velocity, with feasibility determined by constraint functions.

The change in the effect of the moon's gravity from a perturbing force to the central body within the moon's SOI is ignored at this level of fidelity, as the spacecraft is only within the moon's SOI for approximately 5% of the trajectory phase. The instantaneous approximation is similarly justified as the time taken for a gravity assist, around 1 day for each of two gravity assists, is relatively small compared to the entire Earth escape trajectory, with a duration of almost 50 days. The use of these approximations saves several hours of computation time. Modeling the gravity assists by switching to a moon-centered system would add two Sims–Flanagan phases to the model per gravity assist [6], increasing the size of the optimization problem by adding the appropriate decision variables and increasing the time taken to compute these additional phases.

### C. Trajectory Stages

The trajectories presented consist of three different stages, shown in Fig. 2, patched together. Three stages are necessary because the model must switch between three different two-body problems (Earth-centered, sun-centered, and Venus-centered) as the spacecraft passes in and out of the Earth's and Venus's spheres of influence. Each stage has a different central body and different scaling of units. Stages are split further into phases, as in Fig. 1: stage 1 contains three phases, and stages 2 and 3 contain one phase each. The end control node of each phase becomes the start control node of the next.

As the optimization problem becomes large when all stages are considered together, each phase is patched into the optimization problem one at a time, the problem growing to include the new phase in addition to all previous phases each time. Each new phase included in the problem is able to alter all decision variables of all previous phases. Although solving each phase separately, then fixing their endpoints to become the start point to solve the following phase, would make the problem space smaller, the increased flexibility of the unfixed version makes it easier to find feasible solutions. The increased ease of finding a feasible solution also reduces computation time such that the nonfixed solution takes around four or five times less time to solve. Figure 3 shows how the optimization problem increases in size with each new phase in the trajectory.

Stage 1 is the Earth launch-to-escape stage, divided further into three phases. This stage starts following launch with injection onto a lunar intercept trajectory and ends in escape from the Earth's SOI, using two LGAs. The first phase is a coast from injection onto a lunar trajectory to the first LGA. The second phase is a thrust arc from the

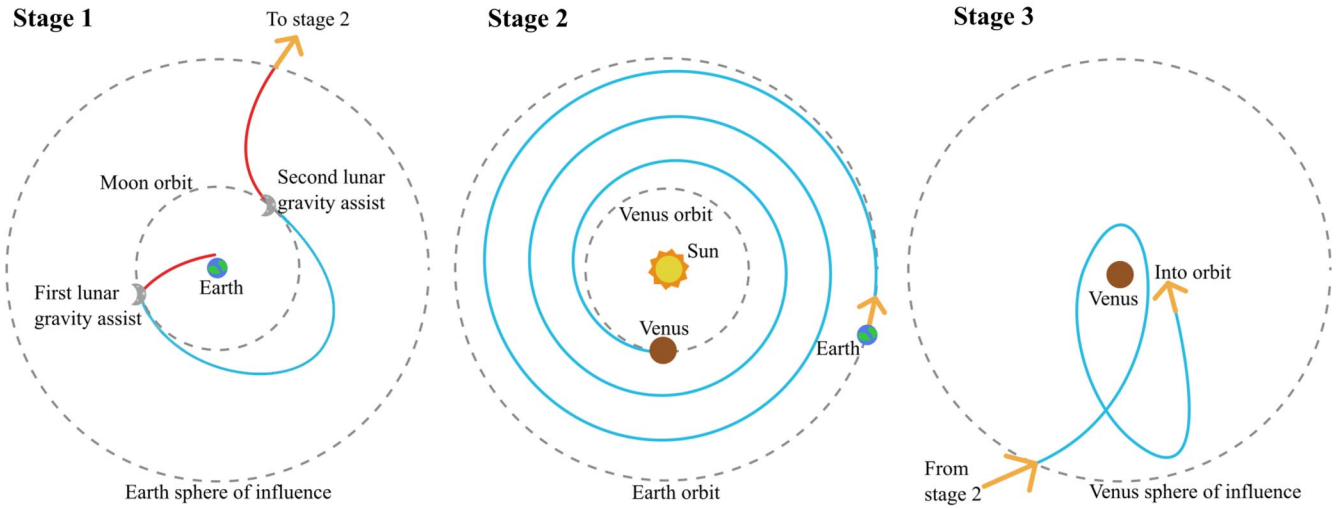


**Fig. 2 Sketch of the three stages of the trajectory solved simultaneously. A dashed line shows a celestial body's orbit or SOI; a blue line shows a thrust arc; a red line shows a coast arc.**

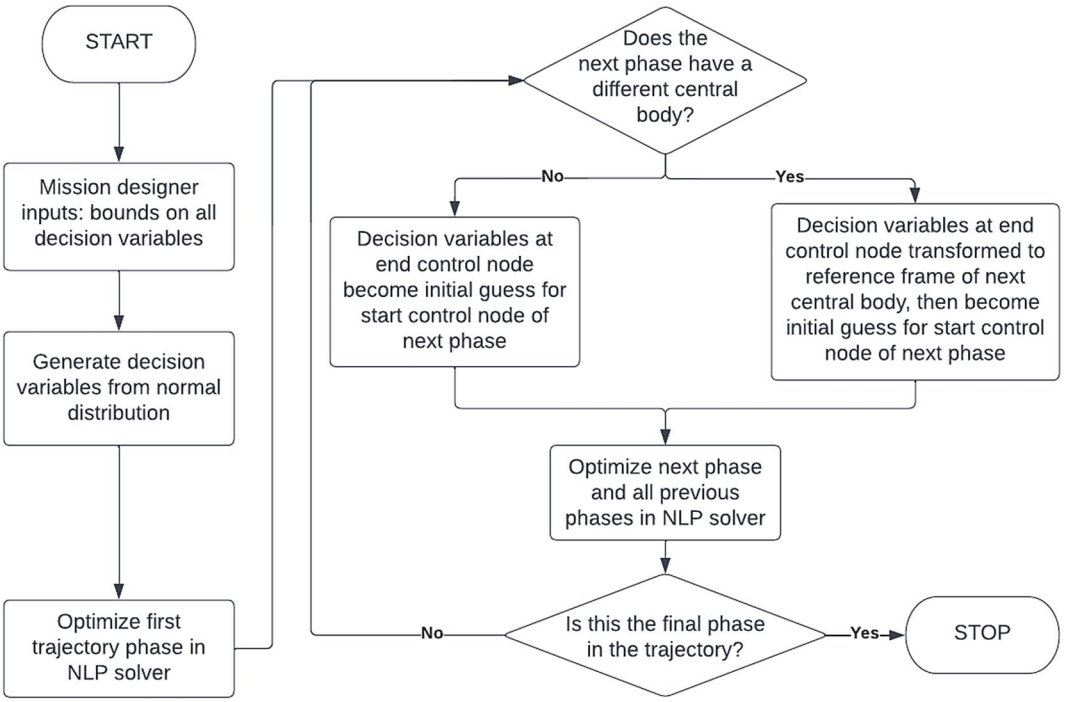


**Fig. 3 Flow diagram showing how the optimization problem grows in size with each new trajectory phase solved, and how the transfer from one phase to the next is done with no manual work.**

first to the second LGA. The third phase is another coast arc, this time from the second LGA to the edge of the Earth's SOI, where the spacecraft is considered to have escaped. Stage 1 is Earth-centered, with gravitational perturbations due to the moon and the sun.

Stage 2 is the interplanetary stage. The final spacecraft state at departure from the Earth's SOI from stage 1 is used as the initial point of stage 2. An endpoint is targeted on the edge of Venus's SOI with a hyperbolic excess velocity relative to Venus of less than 0.5 km/s, to target a capture. Thrust is allowed throughout. The sun is the central body, and the Earth and Venus are perturbing bodies.

Stage 3 is arrival at Venus. The target point from stage 2 is used as the initial point in a Venus-centered arrival trajectory. Stage 3 targets an orbit of eccentricity greater than 0.7 to attempt Venus capture. Such an orbit is not ideal for a science mission. To permit more time close to or within Venus's atmosphere to obtain data for a science mission, with shorter gaps between passes, a low semimajor axis or a circular orbit within the atmosphere would be preferable. Circularizing the orbit requires so many revolutions that the Sims–Flanagan transcription is no longer useful, however. The trajectory would require too many segments, suffering the curse of dimensionality. The greater number of decision variables would increase the problem size beyond reasonable computational cost. Instead, the model attempts capture with a low radius of periapse such that the spacecraft may dip into Venus's atmosphere a few times for scientific observation. Stage 3 is a Venus-centered model, with the sun as the only perturbing body.

Swapping from one stage to the next is done autonomously. Trajectory phases are patched together at their shared control nodes even when changing central body. The growth of the problem as each new phase is added to the problem is shown in Fig. 3. At a control node where the following phase has a different central body to the previous phase, the state vector is transformed from the reference

frame of the previous to the new central body. This is done simply by adding or subtracting the previous central body's position and velocity vector to or from that of the new central body, depending on how the central bodies' position and velocity vectors are defined relative to each other (e.g., the Earth is defined relative to the sun, but the moon is defined relative to the Earth). This requires no additional manual work. All inputs from the mission designer—the definition of bounds on each decision variable, which can be wide so they are not difficult to select, and providing information on the spacecraft engineering specifications—are already obtained before solving the optimization problem.

Units of distance, time, and mass are all scaled in this work, and scaled differently depending on the stage. Distance is scaled according to the distances expected between the spacecraft and central body. For stage 1, this is the moon's average orbital radius. In stage 2, distance is scaled such that 1 AU is one distance unit. For stage 3, it was found that a smaller distance unit was required, so Venus's radius was used. Mass units are constant over all three stages, as the initial spacecraft mass is set to equal one mass unit. The time units are set so that for each stage, the orbital period of an object one distance unit from the central point is $2\pi$ time units. All constraints and decision variables are scaled according to these units.

## III. Solution and Optimization

To search a large problem space for possible solutions, the trajectory is posed as an NLP problem and solved using the sequential quadratic programming (SQP) algorithm within MATLAB's *fmincon* function. The derivatives of the constraints with respect to the decision variables, which form the problem Jacobian, are found by *fmincon* using finite differencing. An aim of this work was to find trajectories with minimal input from a mission designer, so the initial guess for the NLP is generated from a uniform distribution within the bounds on decision variables. These bounds are wide enough not to require detailed knowledge of the system, and to enable numerous locally optimal feasible solutions to be found with a variety of flight times and launch dates. Note that *fmincon* struggles to converge on a feasible solution when given a large number of decision variables, a poor initial guess, and a large search area. To remedy this, an MBH algorithm was used [13,28].

MBH is a basin hopping algorithm. Figure 4 explains the algorithm as a flowchart. It first searches locally around an initial guess by solving the optimization problem with an NLP solver. The optimized solution is then perturbed by perturbations generated from a normal distribution, and re-solved. If a solution found using the perturbed variables is more optimal than the previous solution, this perturbed solution is identified as the new best solution, perturbed again, and solved again. Otherwise, the previous solution is perturbed again and solved again.

The problem to be solved by the optimization algorithm is to minimize the objective function Eq. (16) while satisfying the constraints defined in the following section within the tolerance chosen, which in this study was $1 \times 10^{-6}$ in the normalized units previously described. The decision variables and constraints of the problem to be solved are laid out in the section below. The decision variables are provided to the constraint functions, which are solved by the optimizer.

The objective function in this work maximizes final spacecraft mass. The greater the final mass, the less fuel expended in flight. As *fmincon* always minimizes the objective function, here we minimize the negative value of the final mass to effectively maximize final mass, i.e.,

$$f_{\text{objective}} = -m_{\text{f}} \tag{16}$$

### A. Decision Variables

Decision variables in this model consist of the spacecraft state vector (position, velocity, and mass) in Cartesian coordinates relative to the central body at each control node, the thrust control vector, the spacecraft velocity before and after gravity assists, the initial epoch, and time of flight. Nodes are shared between phases, so the state vector at the final node of one phase is also the state vector at the initial node of the next, reducing the number of decision variables required.

Table 1 shows all of the decision variables used in this model. Decision variables appear with different frequency depending on the number of thrust and coast arcs. There are two coast phases in this model. Final mass and a control vector are not required for those two phases, as mass is constant across these phases and no thrust is present to control. The first and last control nodes of the trajectory are defined by an initial or final orbit by their orbital elements and energy. Two control nodes are gravity assists, where the position vector is the moon's location. At these nodes the velocity vectors, consisting of one decision variable for each of three directions in Cartesian coordinates, are decision variables defined before and after the gravity assist. The two other control nodes are located at the

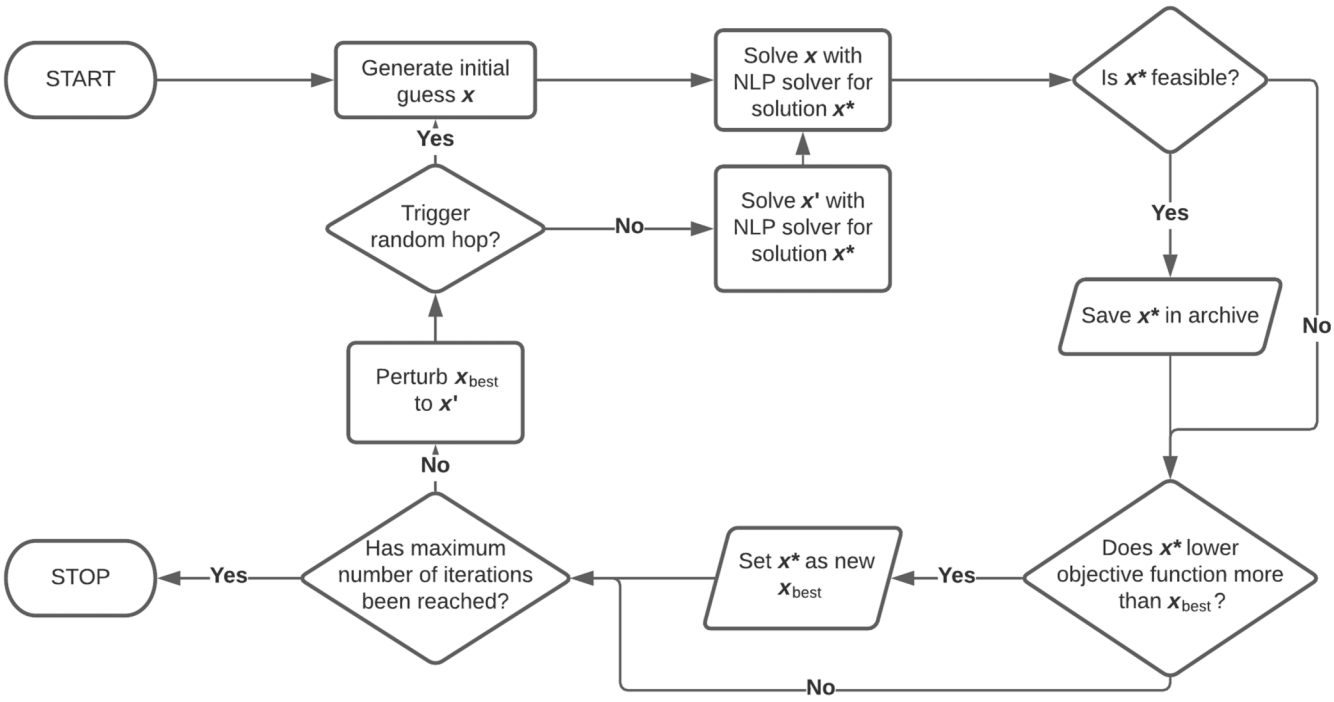


**Fig. 4 Flowchart showing the algorithm used for MBH.**

**Table 1 Decision variables, and how many of each, used**

| Variable | Description | Quantity |
|---|---|---|
| $t_0$ | Launch epoch | 1 |
| $v_\infty$ | Launch impulse magnitude | 1 |
| $E$ | Initial and final orbit characteristic energy | 2 |
| $(\omega, e, i, \Omega, \nu)$ | Initial and final orbital elements (argument of perigee, eccentricity, inclination, and right ascension of ascending node) | 2 each |
| $\Delta t_p$ | Time of flight of phase | $N_p$ |
| $\boldsymbol{v}_{\infty,\mathrm{i}}$ | Excess velocity vector before gravity assist | 6 |
| $\boldsymbol{v}_{\infty,\mathrm{f}}$ | Excess velocity vector immediately after gravity assist | 6 |
| $\boldsymbol{v}_f$ | Velocity vector at nongravity assist control node | 6 |
| $m_f$ | Final phase mass | $N_p - 2$ |
| $\boldsymbol{r}_f$ | Position at nongravity assist control node | 6 |
| $\boldsymbol{u}$ | Control vector | $N(N_p - 2)$ |

spheres of influence of the Earth and Venus, where the system moves between different two-body systems. Here each of the three components of the position and velocity vectors in Cartesian coordinates is a decision variable. The number of phases, and so number of control nodes, is chosen a priori.

### B. Constraints

Nonlinear constraints are enforced by the optimizer to ensure that the trajectory is feasible. The first of these is a core part of the Sims–Flanagan transcription. The forward- and backward-shooting arcs of the trajectory are propagated to a match point halfway through the phase in time, where like any other point in the trajectory there can be no discontinuity in spacecraft position, velocity, or mass. The match point constraint forces continuity by equating the state vectors at the match point:

$$\boldsymbol{c}_{\mathrm{mp}} = \boldsymbol{X}_{\mathrm{B}} - \boldsymbol{X}_{\mathrm{F}} = \begin{bmatrix} \boldsymbol{r}_{\mathrm{B}} - \boldsymbol{r}_{\mathrm{F}} \\ \boldsymbol{v}_{\mathrm{B}} - \boldsymbol{v}_{\mathrm{F}} \\ m_{\mathrm{B}} - m_{\mathrm{F}} \end{bmatrix} = \boldsymbol{0} \tag{17}$$

An additional constraint is that the trajectory thrust profile cannot demand more than the maximum thrust. Thrust magnitude and direction at each segment is controlled by the thrust control vector. To prevent calling for an infeasibly large magnitude of thrust, the up-to-unit vector control prevents the magnitude of the control vector exceeding unity. Physically, this means that the thruster operates for less than 100% of the length of the segment.

$$\|\boldsymbol{u}_k\| = \sqrt{u_{xk}^2 + u_{yk}^2 + u_{zk}^2} \leq 1 \tag{18}$$

The gravity assists are modeled using a patched-conic approximation. The spacecraft velocities relative to the Earth before and after a gravity assist are decision variables. Constraints drive the gravity assist toward feasibility. The first of these enforces conservation of momentum by preventing the spacecraft excess velocity relative to the moon from changing:

$$c_{v_\infty} = v_\infty^+ - v_\infty^- = 0 \tag{19}$$

where $v_\infty^+$ and $v_\infty^-$ are, respectively, the spacecraft excess velocity relative to the moon immediately following and preceding the gravity assist.

Other constraints prevent the spacecraft from dropping below a safe height $h_{\mathrm{safe}}$ above the moon's surface during gravity assists, and ensure that the turn angle is feasible. The turn angle is the angle through which the spacecraft velocity vector relative to the moon turns during a gravity assist:

$$c_{\mathrm{altitude}} = r_{\mathrm{periapse}} \geq r_{\mathrm{body}} + h_{\mathrm{safe}}$$

$$\frac{\mu}{v_\infty^{+2}}\left(\frac{1}{\sin\left(\frac{\delta}{2}\right)} - 1\right) - r_{\mathrm{body}} - h_{\mathrm{safe}} \geq 0 \tag{20}$$

where

$$\delta = \arccos\left(\frac{\boldsymbol{v}_\infty^- \cdot \boldsymbol{v}_\infty^+}{v_\infty^- v_\infty^+}\right) \tag{21}$$

Constraints are also used to help specify the target position of the spacecraft when switching central bodies. These are used to ensure that the final point in the Earth-escape stage is on the edge of the Earth's SOI, and that the final point of the interplanetary stage is on the edge of Venus's SOI when arriving at a Venus capture:

$$c_{\mathrm{escape}} = \|\boldsymbol{r}_{\mathrm{f}_{S1}}\| - r_{\mathrm{SOI_E}} = 0 \tag{22}$$

$$c_{\mathrm{arrival}} = \|\boldsymbol{r}_{\mathrm{f}_{S2}}\| - r_{\mathrm{SOI_V}} = 0 \tag{23}$$

where subscripts S1 and S2 refer to the first (Earth escape) and second (interplanetary, ending in Venus arrival) stages, respectively, and $r_{\mathrm{SOI_E}}$ and $r_{\mathrm{SOI_V}}$ are the radii of the Earth's and Venus's spheres of influence.

## IV. Results

### A. Example Trajectories

Two example trajectories produced by the model are presented here: trajectory A and trajectory B. The goal of this work was to conduct a preliminary search for feasible trajectories, and to demonstrate the capabilities of small spacecraft and the model used. The problem space examined was large, so there are numerous similarly optimal trajectories possible. This work was focused on conducting a preliminary search for feasible trajectories, interested more in finding several feasible trajectories for a given mission, so the solutions did not have to be necessarily the global optimum. Two example trajectories are presented to demonstrate that the method used in this work is capable of finding feasible trajectories when searching a wide problem space, and to suggest the capabilities of small spacecraft to perform interplanetary missions.

Both example trajectories start from a lunar rideshare approaching the moon from Earth, then reach a loose capture around Venus following the three stages described earlier. The bounds set on decision variables allow a wide problem space to be searched. As each stage has such different distance scales and different central bodies, the three stages of each trajectory are presented separately. Table 2 describes the thruster model, as well as giving the initial mass for the system. Figures 5–7 show trajectory A in physical space, Figs. 8–10 the same for trajectory B. Tables 3 and 4 show numerical results for trajectories A and B, respectively, including launch dates and flight times. The endpoint around Venus has been propagated forward in Figs. 7 and 10 in a coast arc to show the path the spacecraft would follow after reaching this point. This shows that the results of each trajectory leave the spacecraft in a weakly captured orbit around Venus.

Trajectory A takes 1362 days, or 3.7 years, to reach its weak capture around Venus. Doing so demands the expenditure of 72.4 kg of fuel.

**Table 2 Initial values for all trajectories**

| Parameter | Value |
|---|---|
| Thruster used | BHT600 Hall thruster |
| Thrust | 39 mN |
| Specific impulse | 1500 s |
| Initial total spacecraft mass | 180 kg |

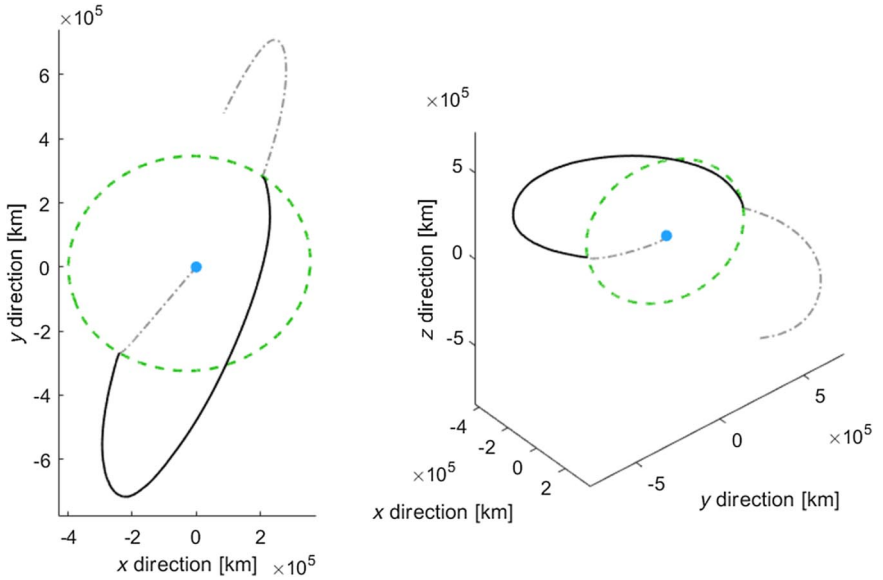


**Fig. 5 Trajectory A, stage 1 (Earth escape), shown from two different perspectives. Earth is a blue dot (not to scale) at the origin. The dashed green circle is the moon's orbit. The black curve shows thrust arcs of the trajectory, and the dot-dashed gray curve shows the coast arcs.**

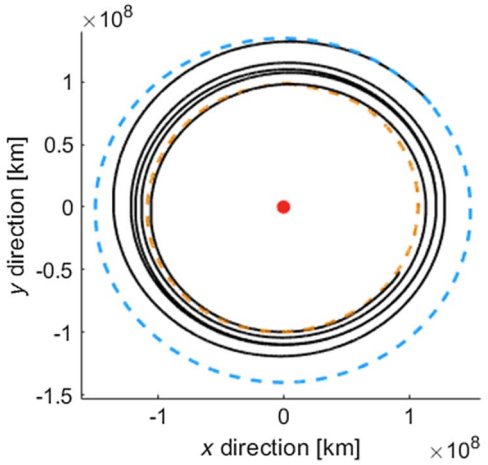


**Fig. 6 Trajectory A, stage 2 (interplanetary), shown in two dimensions as the trajectory is approximately in plane with the sun, Venus, and Earth. The sun is a red dot (not to scale) at the origin. Venus's orbit is shown in orange, and the Earth's orbit in blue. The spacecraft trajectory is in black.**

**Table 3 Numerical results for trajectory A**

| Parameter | Value |
|---|---|
| Final mass | 107.6 kg |
| Launch date | 19th August 2023 |
| Venus arrival date | 27th April 2027 |
| Target orbit arrival date | 12th May 2027 |
| Time of flight | 1,362 days |
| Closest distance to surface of Venus | 104,814 km |
| First LGA $v_\infty$ | 1.50 km/s |
| Second LGA $v_\infty$ | 1.61 km/s |
| Venus arrival $v_\infty$ | 1.40 km/s |

This is not unexpected, as low-thrust systems require a long time to change the spacecraft's orbit to reach targets. Longer flight times mean that more fuel is expended as the thrusters are active for longer. Propagating the spacecraft's final state vector forward in time in a coast arc, seen in Fig. 7, it is evident that the spacecraft will remain in a wide orbit around Venus. This is, however, only likely to remain the case for a small number of orbits before the spacecraft leaves Venus's SOI once more. This is expected because the orbit has such a large eccentricity;

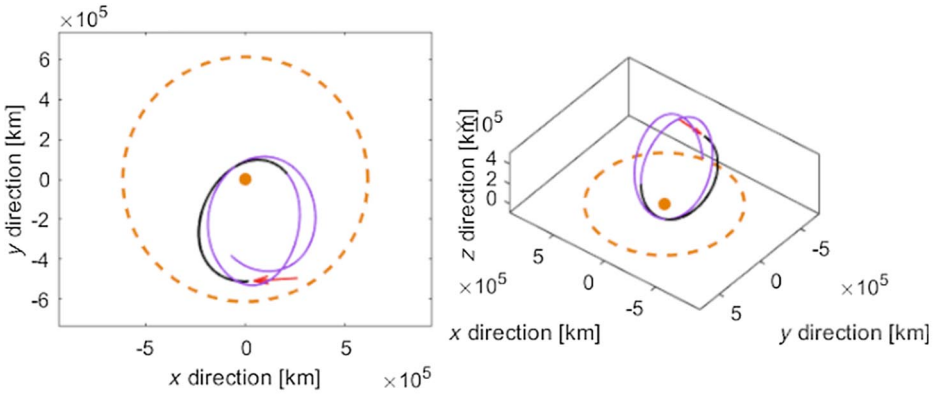


**Fig. 7 Trajectory A, stage 3 (Venus arrival), shown from two different angles. Venus is an orange dot, not to scale, at the origin, and the edge of its SOI is a dashed orange circle. The spacecraft trajectory is shown in black, with a red arrow pointing to the start point. In purple, the trajectory is propagated forward from the endpoint with no thrusting.**

**Table 4 Results for trajectory B**

| Parameter | Value |
|---|---|
| Final mass | 115.7 kg |
| Launch date | 11th July 2024 |
| Venus arrival date | 23rd March 2027 |
| Target orbit arrival date | 11th April 2027 |
| Time of flight | 1,004 days |
| Closest distance to the Venusian surface | 11,052 km |
| First LGA $v_\infty$ | 1.26 km/s |
| Second LGA $v_\infty$ | 1.49 km/s |
| Venus arrival $v_\infty$ | 0.50 km/s |

perturbations due to the sun's gravitational pull have significant effect on the spacecraft at apoapse.

The final orbit, before any coasting is included, passes 104,814 km above Venus's surface at periapse. This is too high to sample the atmosphere. Other observations of Venus could still be made, with several passes of Venus possible before the spacecraft escapes its SOI.

A desirable Venus atmosphere mission would reach within the Venusian atmosphere to take and analyze samples of the atmosphere. Depending on the engineering of the spacecraft, its exposure to the highly damaging conditions of the Venusian atmosphere would require limitation, though this is beyond the scope of this work. Here 100 km above the Venusian surface was assumed to be a minimum safe height. The closest approach of trajectory A is three orders of magnitude greater than this height. While observations could still be made at this height, and remains of interest for a low-thrust spacecraft to reach a weak capture around Venus, improvements can be sought. As will be seen in a later section, these improvements can be achieved using more restrictive constraints on the final radius of periapse.

Trajectory B has a time of flight of 1004 days, or 2.8 years. It expends 64.3 kg of fuel. The final height above Venus at periapse is 11,052 km, much closer than trajectory A for making observations of the planet, but still not good enough for sampling the atmosphere. Propagating the final spacecraft state forward in time, shown in Fig. 10, apoapse does now reach outside the SOI of Venus. Outside Venus's SOI, the sun's gravitational pull dominates over that of Venus, and so the spacecraft is likely to escape Venus sooner than in trajectory A.

The velocity of both trajectories is initially determined by the highly elliptical orbit the spacecraft is launched into to target the moon. Figure 11 shows how the velocity magnitude of both example trajectories evolves over its course. The high spike at the start of each stage 1 trajectory is due to the spacecraft being injected near periapse of a highly elliptical orbit around the Earth. Similarly, peaks toward the end of stage 3 suggest periapse in an orbit around Venus, as the spacecraft enters at a low enough velocity relative to Venus, as seen in Tables 3 and 4, to become weakly captured. In the interplanetary stage 2, deviations from a periodic orbit around the sun are due to thrusting and interactions with the Earth or Venus.

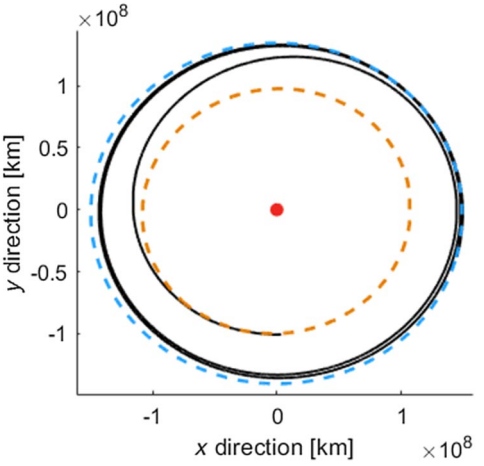


**Fig. 9 Trajectory B, stage 2 (interplanetary), shown in two dimensions as the trajectory is approximately in plane with the sun, Venus, and Earth. The sun is a red dot (not to scale) at the origin. Venus's orbit is shown in orange, and the Earth's orbit in blue. The spacecraft trajectory is in black.**

The $n$-body perturbations had little effect, except that it was found at the edge of a central body's SOI, and perturbations are of the same order of magnitude from this central body and the body it orbits. For example, when crossing into the Venus-centered regime, for the first Sims–Flanagan segment the sun caused changes in velocity of the same order of magnitude as Venus despite being modeled as a perturbation. All feasible solutions found had a similar evolution of velocity, including the difficulty with the SOI boundary.

In Figs. 5–10, coast arcs are shown as gray dot-dashed curves, while thrust arcs are solid black curves. The maximum thrust available here is low such that it takes years to change the spacecraft velocity enough to reach Venus. Once the spacecraft reaches Venus, it enters a coast arc, and Venus's gravity is able to keep the spacecraft in orbit for at least 100 days.

Trajectory A takes 358 days longer to reach Venus than trajectory B, and expends 8.1 kg more fuel. Both examples demonstrate that it is possible for the model described in this work to find a feasible trajectory from a lunar rideshare to an orbit around Venus for a small satellite using low thrust. The model searched a wide parameter space, including a two-year-long launch window and thrust control vectors generated anywhere from 0 (thrusters off) to 1 (thrusters at full force) in any direction. This shows that it is possible to perform low-fidelity searches in this way with little input from a mission designer, and little knowledge of the problem. Maximum power available to the thrusters is assumed to be constant, though in reality would vary with distance to the sun and during events such as eclipses.

The great difference between height above Venus's surface at periapse between trajectory A (104,814 km) and trajectory B

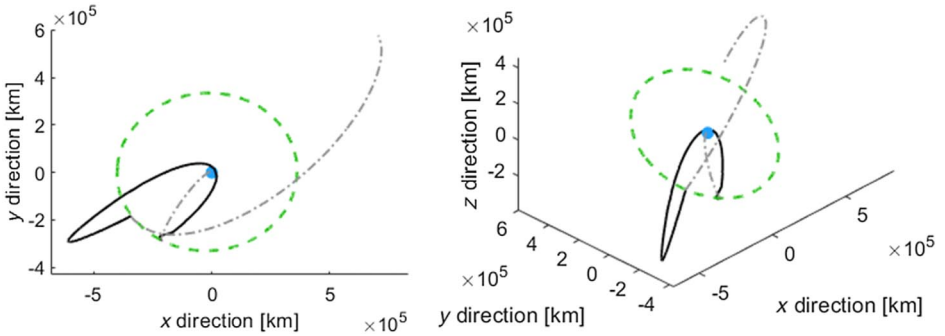


**Fig. 8 Trajectory B, stage 1 (Earth escape), shown from two different perspectives. Earth is a blue dot (not to scale) at the origin. The dashed green circle is the moon's orbit. The black curve shows thrust arcs of the trajectory, and the dot-dashed gray curve shows the coast arcs.**

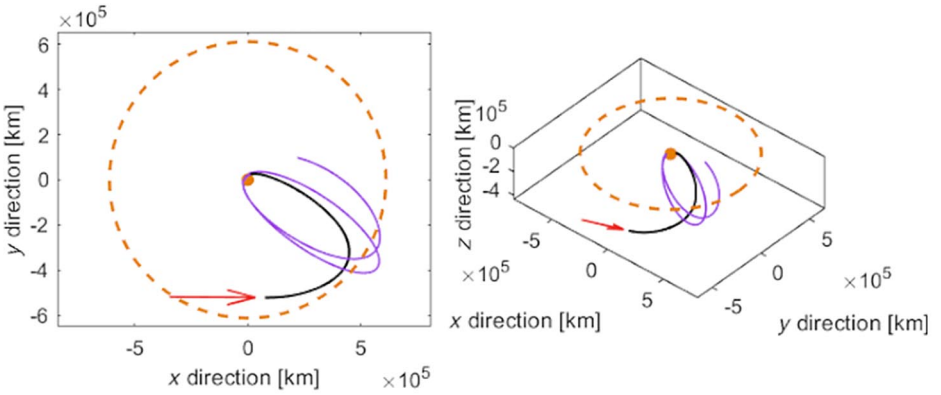


**Fig. 10 Trajectory B, stage 3 (Venus arrival), shown from two different angles. Venus is an orange dot, not to scale, at the origin, and the edge of its SOI is a dashed orange circle. The spacecraft trajectory is shown in black, with a red arrow pointing to the start point. In purple, the trajectory is propagated forward from the endpoint with no thrusting.**



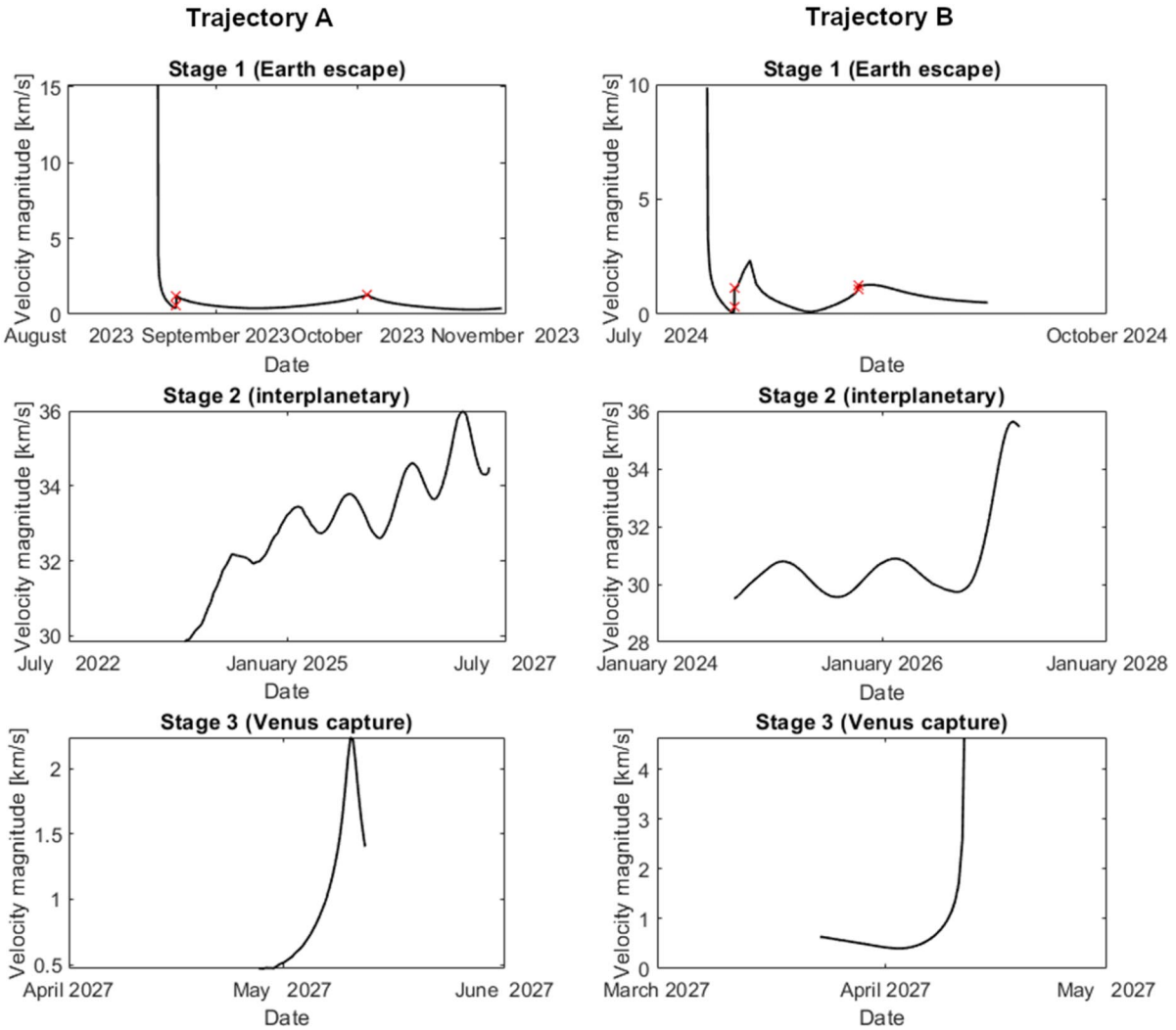


**Fig. 11 The magnitude of spacecraft velocity relative to the central body for each stage of both example trajectories. The central body for stage 1 is the Earth, for stage 2 is the sun, and for stage 3 is Venus. Red crosses in stage 1 indicate the locations of LGAs, where the velocity instantaneously changes due to the gravity assist.**

(11,052 km) demonstrates that the final orbits the spacecraft reaches can vary significantly. The utility of a mission depends on how close, and for how long, the spacecraft can be to objects of scientific interest. For example, by reducing proximity to a few hundred kilometers, the spacecraft may be able to take direct measurements of the dense atmosphere of Venus.

### B. Tradeoff Between Final Mass and Proximity to Venus

Having observed great differences in final proximity to Venus in the previous section, the tradeoff between final spacecraft mass (and so, fuel expenditure) and the height above Venus of the spacecraft at the periapse of its final orbit was explored. For some missions, a specific final height margin may exist within which the spacecraft

risks destruction by Venus's hostile environment, above which useful measurements cannot be taken. In general, it was assumed that approaching as close to Venus's surface as possible was preferable.

Several searches for trajectories were conducted. Each search had a different upper bound on final spacecraft mass, to force a spread of final mass values in order to search for any trends in a relationship between final minimum height above Venus and final mass. Figure 12 presents the feasible results from these searches. There is no trend of note. Although the trajectories with higher final mass were able to achieve periapses closer to Venus, there is a large spread in the data and fewer trajectories found at lower final masses.

No noted tradeoff between fuel expenditure and final proximity to Venus is encouraging to Venus missions. Lower fuel costs leave a greater mass budget for launching scientific equipment. This result implied that restricting the final proximity to Venus in the optimizer was possible at little to no fuel cost, and so further investigations were undertaken.

Searches optimizing for minimum final radius of periapse, instead of maximum final mass, were conducted to investigate this tradeoff further. It was found that the model can readily converge on feasible solutions with a final radius of periapse of only a few hundred kilometers above Venus's surface. Trajectories reaching low heights above Venus were found consistently. The final masses found when radius of periapse is the objective function have a similar range, but slightly smaller values, to those seen in Fig. 12 were possible, and enforced by changing the bounds on the final mass decision variable. To further this, an extra constraint restricting the final radius of periapse between a minimum safe value of 100 km and a chosen maximum value was introduced to the optimization problem seeking to maximize final mass. The maximum value was set to 500, 1000, and 5000 km for different runs of the search. Each time, computation time was a few hours longer than without this constraint, but a similar number of feasible trajectories were found.

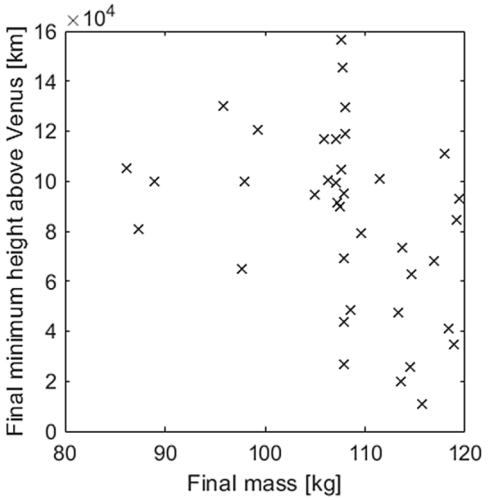


**Fig. 12 The height above the surface of Venus at periapse of the final orbits with respect to the final mass of the spacecraft for different feasible trajectories found in global searches for lunar-rideshare-to-Venus trajectories.**

An example of stage 3, the Venus arrival stage, for a trajectory with final periapse bound between 100 and 500 km above Venus's surface, is shown in Fig. 13. The total flight time from Earth to Venus is 607 days (1.7 years), and the final mass is 116 kg. The closest approach to Venus's surface here is 500 km, similar to other trajectories with these bounds, suggesting that the optimizer does tend toward its upper limit for radius of periapse. Further investigation could confirm this, but there is still no apparent link between this and final mass. Propagating the trajectory beyond its final point in Fig. 13 finds that the trajectory leaves Venus's SOI, so is likely to escape its orbit after a few passes around Venus.

It is likely that there is no observed tradeoff between final mass and final proximity to Venus because the final orbit has a large eccentricity and semimajor axis. Apoapse can remain close to the edge of Venus's SOI, from where the spacecraft arrives, and so little change to the spacecraft arrival state needs to be made to result in an orbit with a given radius of periapse. The spacecraft is still at risk of leaving Venus's SOI, as in Figs. 10 and 13, escaping Venus sooner. Highly eccentric orbits as seen here spend less time at periapse, in this case a few hours, providing less time for taking observations. It may be possible to form a multi-objective function to optimize for both final mass and proximity to Venus, and this exploration has seen that it is possible to impose additional constraints on arrival orbit with some cost to computation time. A Pareto front showing the highest final masses possible for a given final proximity to Venus could be obtained by generating solutions from the same seed and applying an apoapse constraint.

### C. Validation of Results

To verify the model used, the model was tested against trajectories existing in literature. Being able to reproduce trajectories in literature would indicate that the model in this work is capable of producing feasible low-thrust trajectories. Being able to find trajectories with similar final masses would indicate that the model used here performs well finding optimal trajectories, where final mass is the objective function.

Figure 14 shows a solution to a trajectory based on one produced for the canceled Asteroid Redirect Robotic Mission (ARRM) mission. This is an Earth-escape section of a full ARRM trajectory using two LGAs, following injection onto the first LGA [29]. This was chosen due to its similarity to the first stage of the problem in this

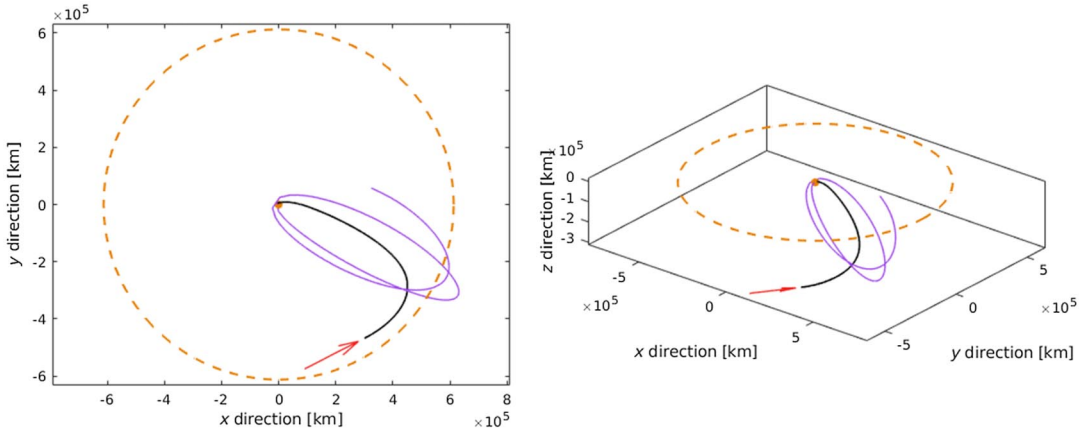


**Fig. 13 A Venus arrival trajectory, shown from two different angles. Venus is an orange dot, not to scale, at the origin, and the edge of its SOI is a dashed orange circle. The spacecraft trajectory is shown in black, with a red arrow pointing to the start point. In purple, the trajectory is propagated forward from the endpoint with no thrusting.**

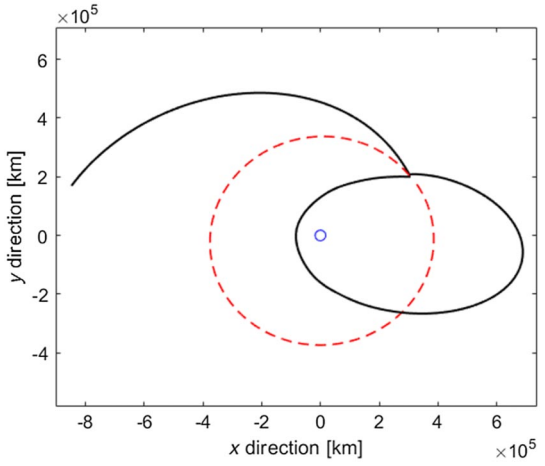


**Fig. 14 Potential ARRM trajectory found using the model used in this work. The Earth is the blue circle at the origin, not to scale. The moon's orbit is the red dashed circle. The trajectory is the solid black curve and is coasting.**

work. The trajectory in literature starts at its first LGA on 14th May 2018, with an altitude of 5523 km and a $v_\infty$ of 0.974 km/s. It reaches its second LGA on 11th June 2018 with an altitude of 60 km and a $v_\infty$ of 1.05 km/s. The trajectory is entirely a coast arc. The solution in Fig. 14 begins with its first LGA on 14th May 2018, which has an altitude of 5371 km and a $v_\infty$ of 0.977 km/s. It reaches its second LGA on 10th June 2018, with an altitude of 41.59 and a $v_\infty$ of 1.027 km/s.

Being able to find a feasible trajectory close to a trajectory designed in literature for a different mission with a similar scenario to stage 1 suggests at least the Earth-centered stage of the model functions to find feasible trajectories. The trajectory found in Fig. 14 is close enough to the trajectory presented by Strange et al. [29] to be the same solution, allowing for slight differences due to approximations such as only including perturbations due to the moon and sun where they include perturbations from more bodies. However, as the Earth-escape portion of the ARRM trajectory was entirely a coast arc, it cannot be used to compare optimality.

Figure 15 shows a possible trajectory for the Jupiter Icy Moons Orbiter (JIMO) mission, for which there is a known globally optimal trajectory [11]. The trajectory begins with escape from the Earth, undergoes an Earth gravity assist, and then travels to rendezvous with Jupiter. This reference trajectory was chosen from the literature to validate the model used in this work because it is interplanetary, so can test the interplanetary regime of the model used in this work, and

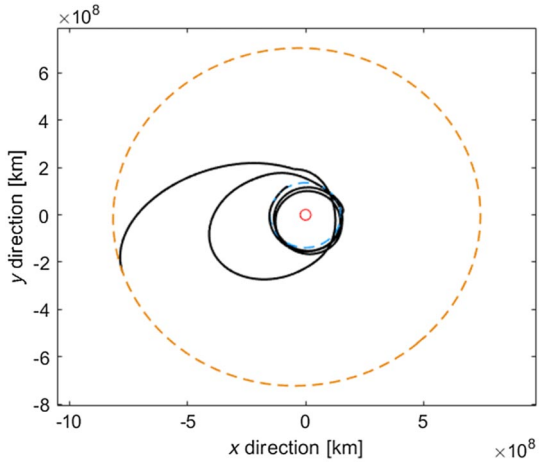


**Fig. 15 Potential JIMO trajectory found using the model used in this work. The red circle at the origin is the sun, not to scale. The blue dashed circle is the Earth's orbit, the orange dashed circle is Jupiter's orbit, and the solid black curve is the spacecraft trajectory.**

because it has a known global optimum, the ability of the model used in this work to find optimal trajectories can be tested.

The JIMO trajectory produced by the model from this work leaves the Earth on 19th January 2021 and reaches the Earth for its gravity assist after 2.68 years on 24th September 2023. The spacecraft arrives at Jupiter after 5.41 years on 20th February 2029. It leaves the Earth with an initial $v_\infty$ of 0.936 km/s, and the $v_\infty$ of its gravity assist is 7.53 km/s. Its minimum altitude above the Earth is 500.0 km. The final mass is 17,149 kg. The known global optimum has a final mass of 17,102 kg. Finding a trajectory close in its objective function, the final mass, to the known global optimum suggests that the model described in this work may be capable of finding global optima. The solution found by the model used in this work is slightly higher than the global optimum, likely due to the assumptions made, for example, the bounded-impulse approximation of continuous thrust and the assumption that the Earth and Jupiter are the only perturbing bodies in this sun-centered trajectory.

### D. Discussion of Results

The model could consistently find solutions to the lunar-rideshare-to-Venus problem, though only 9.5% of the solutions produced by each MBH run were feasible. Without moons to aid in gravity assists, it is more difficult to reduce the velocity of the spacecraft relative to Venus to the extent it becomes captured. Restricting bounds to permit only Venus excess velocities of at most 0.5 km/s was necessary to find solutions. The tradeoff is a longer flight time in stage 2, and fewer solutions found in stage 2.

Perturbations due to $n$-body gravity caused problems when within a few thousand kilometers, or especially when outside, of the boundary of a body's SOI. In this region, the model attempts to approximate a non-Keplerian system as two-body Keplerian, and so the physical approximations become unreliable. Outside the SOI, the perturbing body becomes the dominant force over the central body, but is still modeled as a perturbation. This causes the model to fail to solve for a feasible thrust profile that can counter the force of the now dominant third body, resulting in escape from the celestial body or an infeasible trajectory. This problem occurs at the interface between the interplanetary and Venus capture stages. It can be reduced by targeting an orbit with apoapse less than 90% of the SOI radius from Venus, as this drives the trajectory away from the SOI.

The model used in this work performs a global search. Its solutions, including the example trajectories in this work, can be upgraded to higher fidelity to bring the trajectories closer to flight fidelity, and to examine the approximations made in the model [6]. High-fidelity models do not make the patched conic or bounded impulse approximations as has been done here. Transferring a patched conic LGA to a full propagation in the moon-centered two-body problem removed this approximation, but the conversion can be difficult [30]. Additional improvements to fidelity can be made by implementing a power system model [31]. This work assumed constant power available to the spacecraft's thrusters, so a constant maximum thrust, as traveling closer to the sun will only make more power available to solar-powered systems. In reality, the maximum power available may be more significantly variable.

The spacecraft considered here had a mass of 180 kg. This is small compared to other interplanetary spacecraft, which can be several tons, but significantly larger than the tens of kilograms seen in smaller spacecraft such as CubeSats. Launching spacecraft of less mass is generally cheaper, so applying this model to CubeSats would improve accessibility of interplanetary space to those without the resources to build large-scale spacecraft.

This work used MATLAB's *fmincon* function to solve the NLP, without taking advantage of the sparsity of the problem. Another solver such as SNOPT [32] could be used to solve the problem and can be supplied the sparsity pattern, possibly finding solutions faster. This work uses finite differencing to solve the NLP problem. Using analytical derivatives [33] could also improve the accuracy of solutions [31].

The goal of reaching Venus was achieved, but improvements could be made to the final orbits. These loosely captured orbits are readily

found by the optimizer, as by finding semimajor axes large enough to reach the edge of Venus's SOI, the entry point of the spacecraft into Venus's SOI could be close to a point on the final orbit. With such large semimajor axes and high eccentricities, passes close to Venus are several days or weeks apart, and only last a few hours. It was shown that by introducing constraints on the final radius of periapse over Venus, closer proximity can be achieved with no cost to fuel use. However, many of these closer orbits had apoapses outside Venus's SOI. Outside Venus's SOI, the sun's gravity is the dominant force, pulling the spacecraft away from Venus sooner than it would otherwise.

To increase the time spent close to Venus, the orbit could be circularized and have its apoapse lowered closer to Venus. This could be done by greatly increasing the number of segments and flight times of stage 3. However, this then suffers the curse of dimensionality; as more segments means many more decision variables, and each one adds a state vector and thrust control. The problem would then become computationally expensive, and could struggle to find solutions in so large a problem space, so other methods could be explored [34]. Other maneuvers exist that may not require such computational expense as thrusting is limited to small arcs near periapse directed opposite the velocity vector. When passing through Venus's atmosphere, atmospheric drag will have an effect not explored in this work, which may be able to lower apoapse.

In this work, the challenging mission design problem of an Earth–Venus trajectory for a low-thrust spacecraft has been successfully solved using patched adapted Sims–Flanagan trajectory arcs. Although the solutions could be improved by circularization, the solutions found can still be of use for scientific missions. The trajectories still permit spacecraft to reach close to the Venusian atmosphere when constraints are placed on the final closest approach to the surface of Venus. The model and optimization methods used in this work can also be applied to other planetary targets. Venus was chosen as the target due to interest in studying its atmosphere and topography, but other bodies in the solar system could be targeted, possibly with the addition of planetary gravity assists in stage 2.

## V. Conclusions

In this work, a preliminary search for low-thrust trajectories to Venus from a lunar rideshare was conducted. By patching together Sims–Flanagan-based trajectories in three regimes, it was possible to find feasible trajectories from injection onto a lunar trajectory to weak capture at Venus. Example trajectories demonstrate the possibility of achieving this using two LGAs, followed by spiraling around the sun until the spacecraft arrives at a final weak capture around Venus. A search through a large problem space was performed using NLP with an MBH algorithm. The trajectory model is based on the Sims–Flanagan transcription to approximate continuous thrust as a series of impulses in an otherwise two-body Keplerian problem, and includes $n$-body perturbations due to the gravitational forces of the Earth, moon, Venus, and the sun. The result is a low-fidelity optimizer that produces solutions that can be used as an initial guess by a higher-fidelity optimizer. By utilizing gravity assists, it has been shown that even without their own dedicated launch, it is possible for missions using small spacecraft and low thrust to reach interplanetary targets. Searches for trajectories reaching different proximities to Venus reveal that it is possible to specify missions reaching close to or within Venus's upper atmosphere with little or no cost to final mass, though some cost to computation time.

## Acknowledgments

This work used NASA's SPICE toolkit for ephemeris data. The work was supported by a University of Auckland Doctoral Scholarship. The authors would like to thank Christopher Scott for useful feedback, and Daniel Miller for helpful discussions. The authors would also like to thank the anonymous reviewers for their comments, which helped to significantly improve the quality of this work.

## References

[1] Strange, N., Landau, D., Hofer, R., Snyder, J. S., Randolph, T., Campagnola, S., Szabo, J., and Pote, B., "Solar Electric Propulsion Gravity-Assist Tours for Jupiter Missions," *AIAA/AAS Astrodynamics Specialist Conference*, AIAA Paper 2012-4518, 2012. https://doi.org/10.2514/6.2012-4518

[2] Kane, S. R., Arney, G., Crisp, D., Domogal-Goldman, S., Glaze, L. S., Goldblatt, C., Grinspoon, D., Head, J. W., Lenardic, A., Unterborn, C., Way, M. J., and Zahnle, K. J., "Venus as a Laboratory for Exoplanetary Science," *Journal of Geophysical Research: Planets*, Vol. 124, No. 8, 2019, pp. 2015–2028. https://doi.org/10.1029/2019JE005939

[3] Sundararajan, V., "Tradespace Exploration of Space System Architecture and Design for India's Shukrayaan-1, Venus Orbiter Mission," *ASCEND*, AIAA Paper 2021-4103, 2021. https://doi.org/10.2514/6.2021-4103

[4] Glaze, L., Garvin, J., Robertson, B., Johnson, N., Amato, M., Thompson, J., Goodloe, C., and Everett, D., "DAVINCI: Deep Atmosphere Venus Investigation of Noble Gases, Chemistry, and Imaging," *IEEE Aerospace Conference*, Inst. of Electrical and Electronics Engineers, New York, 2017, pp. 1–5.

[5] Freeman, A., Smrekar, S., Hensley, S., Wallace, M., Sotin, C., Darrach, M., Xaypraseuth, P., Helbert, J., and Mazarico, E., "VERITAS—A Discovery-Class Venus Surface Geology and Geophysics Mission," *11th Low Cost Planetary Missions Conference*, Inst. of Electrical and Electronics Engineers, New York, 2016, pp. 1–11.

[6] Graham, D. R., Englander, J. A., Rattenbury, N. J., and Cater, J. E., "Low-Thrust Venus Trajectories at Low and High Fidelity," *AAS/AIAA Astrodynamics Specialist Conference*, AAS Paper 21-571, 2021.

[7] Breakwell, J. V., "The Optimization of Trajectories," *Journal of the Society for Industrial and Applied Mathematics*, Vol. 7, No. 2, 1959, pp. 215–247. https://doi.org/10.1137/0107018

[8] Jezewski, D. J., "Primer Vector Theory and Applications," NASA TR-R454, 1975.

[9] Enright, P. J., and Conway, B. A., "Discrete Approximations to Optimal Trajectories Using Direct Transcription and Nonlinear Programming," *Journal of Guidance, Control, and Dynamics*, Vol. 15, No. 4, 1992, pp. 994–1002. https://doi.org/10.2514/3.20934

[10] Tang, S., and Conway, B. A., "Optimization of Low-Thrust Interplanetary Trajectories Using Collocation and Nonlinear Programming," *Journal of Guidance, Control, and Dynamics*, Vol. 18, No. 3, 1995, pp. 599–604. https://doi.org/10.2514/3.21429

[11] Yam, C. H., Lorenzo, D. D., and Izzo, D., "Low-Thrust Trajectory Design as a Constrained Global Optimization Problem," *Proceedings of the Institution of Mechanical Engineers, Part G: Journal of Aerospace Engineering*, Vol. 225, No. 11, 2011, pp. 1243–1251. https://doi.org/10.1177/0954410011401686

[12] Vasile, M., Minisci, E., and Locatelli, M., "Analysis of Some Global Optimization Algorithms for Space Trajectory Design," *Journal of Spacecraft and Rockets*, Vol. 47, No. 2, 2010, pp. 334–344. https://doi.org/10.2514/1.45742

[13] Englander, A. C., Englander, J. A., and Carter, M. J., "Hopping with an Adaptive Hop Probability Distribution," *27th AAS/AIAA Space Flight Mechanics Meeting*, AAS Paper 20-484, 2020.

[14] Petropoulos, A., and Longuski, J., "Shape-Based Algorithm for the Automated Design of Low-Thrust, Gravity Assist Trajectories," *Journal of Spacecraft and Rockets*, Vol. 41, No. 5, 2004, pp. 787–796. https://doi.org/10.2514/1.13095

[15] Belbruno, E. A., and Miller, J. K., "Sun-Perturbed Earth-to-Moon Transfers with Ballistic Capture," *Journal of Guidance, Control, and Dynamics*, Vol. 16, No. 4, 1993, pp. 770–775. https://doi.org/10.2514/3.21079

[16] Howell, K. C., Barden, B. T., Wilson, R. S., and Lo, M. W., "Trajectory Design Using a Dynamical Systems Approach with Application to GENESIS," *AIAA/AAS Astrodynamics Specialist Conference*, AIAA, Reston, VA, 1997, pp. 1665–1681.

[17] Cox, A., Howell, K., and Folta, D., "Dynamical Structures in a Low-Thrust, Multi-Body Model with Applications to Trajectory Design," *Celestial Mechanics and Dynamical Astronomy*, Vol. 131, No. 12, 2019, pp. 1–34. https://doi.org/10.1007/s10569-019-9891-7

[18] Holt, H., Armellin, R., Scorsoglio, A., and Furfaro, R., "Low-Thrust Trajectory Design Using Closed-Loop Feedback-Driven Control Laws and State-Dependent Parameters," *AIAA Scitech 2020 Forum*, AIAA Paper 2020-1694, 2020. https://doi.org/10.2514/6.2020-1694

[19] Taheri, E., and Abdelkhalik, O., "Shape-Based Approximation of Constrained Low-Thrust Space Trajectories Using Fourier Series," *Journal*

*of Spacecraft Rockets*, Vol. 49, No. 3, 2012, pp. 535–545. https://doi.org/10.2514/1.A32099

[20] Hatten, N., and Russell, R., "Comparison of Three Stark Problem Solution Techniques for the Bounded Case," *Celestial Mechanics and Dynamical Astronomy*, Vol. 121, No. 1, Jan. 2015, pp. 39–60. https://doi.org/10.1007/s10569-014-9586-z

[21] Englander, J. A., Ellison, D. H., and Conway, B. A., "Global Optimization of Low-Thrust, Multiple-Flyby Trajectories at Medium and Medium-High Fidelity," *AAS/AIAA Space Flight Mechanics Meeting*, AIAA, Reston, VA, 2014, pp. 1539–1558.

[22] Sims, J. A., and Flanagan, S. N., "Preliminary Design of Low-Thrust Interplanetary Missions," *AAS/AIAA Astrodynamics Specialist Conference*, AAS Paper 99-0328, 1999.

[23] Battin, R. H., *Introduction to the Mathematics and Methods of Astrodynamics*, AIAA, Reston, VA, 1999, pp. 464–466.

[24] Der, G. J., "An Elegant State Transition Matrix," *Journal of the Astronautical Sciences*, Vol. 45, No. 4, Dec. 1997, pp. 371–390. https://doi.org/10.1007/BF03546398

[25] Conway, B. A., "An Improved Algorithm Due to Laguerre for the Solution of Kepler's Equation," *Celestial Mechanics*, Vol. 39, No. 2, 1986, pp. 199–211. https://doi.org/10.1007/BF01230852

[26] Acton, C. H., "Ancillary Data Services of NASA's Navigation and Ancillary Information Facility," *Planetary and Space Science*, Vol. 44, No. 1, 1996, pp. 65–70. https://doi.org/10.1016/0032-0633(95)00107-7

[27] Acton, C., Bachman, N., Semenov, B., and Wright, E., "A Look Toward the Future in the Handling of Space Science Mission Geometry," *Planetary and Space Science*, Vol. 150, Jan. 2017, pp. 9–12. https://doi.org/10.1016/j.pss.2017.02.013

[28] Wales, D. J., and Doye, J. P. K., "Global Optimization by Basin-Hopping and the Lowest Energy Structures of Lennard-Jones Clusters Containing up to 110 Atoms," *Journal of Physical Chemistry A*, Vol. 101, No. 28, 1997, pp. 5111–5116. https://doi.org/10.1021/jp970984n

[29] Strange, N., Landau, D., McElrath, T., Lantoine, G., Lam, T., McGuire, M., Burke, L., Martini, M., and Dankanich, J., "Overview of Mission Design for NASA Asteroid Redirect Robotic Mission Concept," *33rd International Electric Propulsion Conference*, IEPC-2013-321, 2013.

[30] Englander, J. A., Folta, D. C., and Hur-Diaz, S. H., "Optimization of the Lunar IceCube Trajectory Using Stochastic Global Search and Multi-Point Shooting," *27th AAS/AIAA Space Flight Mechanics Meeting*, AAS Paper 20-435, 2020.

[31] Ellison, D. H., Conway, B. A., Englander, J. A., and Ozimek, M. T., "Application and Analysis of Bounded-Impulse Trajectory Models with Analytic Gradients," *Journal of Guidance, Control, and Dynamics*, Vol. 41, No. 8, 2018, pp. 1700–1714. https://doi.org/10.2514/1.G003078

[32] Gill, P. E., Murray, W., and Saunders, M. A., "SNOPT: An SQP Algorithm for Large-Scale Constrained Optimization," *SIAM Review*, Vol. 47, Feb. 2005, pp. 99–131. https://doi.org/10.1137/S0036144504446096

[33] Ellison, D. H., Conway, B. A., Englander, J. A., and Ozimek, M. T., "Analytic Gradient Computation for Bounded-Impulse Trajectory Models Using Two-Sided Shooting," *Journal of Guidance, Control, and Dynamics*, Vol. 41, No. 7, 2018, pp. 1449–1462. https://doi.org/10.2514/1.G003077

[34] Shannon, J. L., Ellison, D., and Hartzell, C. M., "Exploration of Low-Thrust Lunar Swingby Escape Trajectories," *31st AAS/AIAA Space Flight Mechanics Meeting*, AAS Paper 21-273, 2021.

J. Parish
*Associate Editor*